Numerical Modeling of the Hydrothermal System at East Pacific Rise 9°50'N Including Anhydrite Precipitation

Kannikha Parameswari Kolandaivelu

Thesis submitted to the faculty of the Virginia Polytechnic Institute and State University
in partial fulfillment of the requirements for the degree of

Master of Science
In
Geosciences

Robert P. Lowell, Chair
Thomas J Burbey
Scott King

23 June 2015
Blacksburg, VA

Keywords: East Pacific Rise, seafloor hydrothermal system, numerical modeling, anhydrite precipitation

Numerical Modeling of the Hydrothermal System at East Pacific Rise 9°50'N Including Anhydrite Precipitation

Kannikha Parameswari Kolandaivelu

ABSTRACT

Seafloor hydrothermal systems have been intensively studied for the past few decades; however, the location of recharge zones and details of fluid circulation patterns are still largely uncertain. To better understand the effects of anhydrite precipitation on hydrothermal flow paths, we conduct 2-D numerical simulations of hydrothermal circulation at a mid-ocean ridge using a NaCl-H_2O numerical code. The simulations focus on East Pacific Rise hydrothermal system at 9°50'N due to availability of key observational data to constrain the models. Seismicity data that is available suggests that fluid flow is primarily along axis and that recharge is focused into a small zone near a 4^{th} order discontinuity in the ridge axis.

Simulations are carried out in an open-top square box 1500 m on a side maintained at a surface pressure of 25 MPa, and nominal seawater temperature of 10 °C. The sides of the box are assumed to be impermeable and insulated. A constant temperature distribution is maintained along the bottom of the box consisting of a 1000 m long central-heated region maintained at 450 °C to represent the axial magma chamber and ensure P-T conditions for phase separation; a linearly decreasing temperature profile from 450 to 300 °C is maintained along the 250 m long segments adjacent to the heated region to delineate the recharge zone. We constructed a homogeneous model with a uniform cell size of 25 m with a permeability of 10^{-13} m^2 and a similar model with a 200 m thick layer 2A region with a permeability of 10^{-12} m^2. For the homogeneous model the

simulations were run for 100 years to approximate steady state conditions and the model with layer 2A was run for 50 years. Assuming that anhydrite precipitation resulted from the decrease in solubility with increasing temperature as downwelling fluid gets heated, the rate of porosity decrease and sealing time was calculated at 50 and 100 years. The results showed that sealing occurred most rapidly at the bottom of the recharge areas near the base of the high-temperature plumes, where complete sealing occurred after ~55-625 years for an initial porosity of 0.1. The simulations also suggested that sealing would occur more slowly at the margins of the ascending plumes, with times ranging between ~ 80 and 5000 years.

The sealing times in the deep recharge zone determined in these simulations are considerably greater than estimated from 1D analytical calculations, suggesting that with a 2D model, focused recharge at the EPR 9°50'N site may occur, at least on a decadal time scale. More detailed analyses are needed to determine whether such focused recharge can be maintained for longer times.

To my Mother and Father, Roberto and The Universe

Acknowledgements

I would like to thank my advisor, Dr. Robert P. Lowell, The Universe, Department of Geosciences, Virginia Tech and other co-conspirators for bringing me to Virginia Tech so that I can fulfill one of my life's dreams of studying Geosciences. This research was supported in part by NSF Grant OCE 1353114 to Robert P. Lowell. I am extremely grateful to the support given by Connie Lowe and Mary McMurray during the times when I needed it a lot. I thank Ellen Mathena, Jo Thomason and Sharon Collins for their help with my various forms. I thank all my teachers at the department who gave me an insight into their worlds of Geosciences and made me more knowledgeable than I was when I arrived in Blacksburg. I thank Llyn Sharp for her co-operation in everything I did related to the museum.

I am extremely grateful to my advisor, Dr. Robert P. Lowell for his suggestions, advice, for his time spent on discussions with me regarding this research and his valuable comments. I also thank him for his support and strength during trying and difficult times. I could not have done this without his support.

I also thank my committee members Dr. Scott King and Dr. Thomas Burbey for their insights and thoughts on this work and also for helping me expand my knowledge beyond just the lines of this project. The department gave me an amazing opportunity to teach the labs and I got to teach a wonderful group of undergraduates most of whom really enjoyed my teaching. I am really thankful for that experience. Thanks to Jim Langridge, Mark Lemon and James Dunson who always solved my computer issues and made this research possible. Thanks to Shreya Singh on helping me start off with FISHES. Special

thanks to Connie Lowe, Dr. Ken Eriksson, Dr. Nancy Ross, Dr. Robert P. Lowell, Dr. Esteban Gazel and Dr. Robert Weiss for giving me their full support when a personal emergency demanded my presence in my home country, India, during my third semester here (Fall 2014).

Graduate life without coffee is like trying to breathe with no oxygen. I thank Nikki, Lexi and my other friends from Seattle's Best in Johnson's Student Center for making me the best coffees ever. I also thank Nick and other friends from Subway for making me smile even when I was pressured with work.

A very special thanks is in order for my wonderful friends at office and outside for accepting me as ME and bringing out the best and worst in me. Thank you Pavithra Sekhar for EVERYTHING for without you I would have been lost. Thank you Aida Farough for all your little acts of kindness and support. Thanks to Dave Mercier, Jing and Kai, Didem Beskardes, Aaron Prunty, Shangxin Liu, Zhen Guo, Qimin Wu, Lulu, Panda, Anna Hardy, Lindsey Sabey, Amir Zainali, Pilar Madrigal, Hector LaMadrid, Jen Gorce and Vanessa Frost for being a part of my two years here and giving me awesome memories to cherish. Thank you to Monika Kodrycka for always having faith in me and my capabilities.

I am thankful to Kayla Lewis without whom this research on FISHES would have just been another fiction of imagination.

Thank you to Shreya Roy Choudhury, Lourdes Escobar and her family, Sherin Fathy, Shadi Es, Moh Bright and my other eclectic partyers for appreciating me for what I am. Sisters don't have to be of blood. I thank my sister Patsy Felice (Erika) for her relentless support and concern. I thank my other sister, Lily Virguez for her advice and support. I

thank my Tiger Sista, Pavithra Sekhar for EVERYTHING. I thank my sister Rosi Maia for being another awesome person.

Mothers are amazing. Super Moms are super amazing. To some of the strong amazing mothers I know: Tahere, Malgorzata (Mamusia), Mari Reme (Super super Mom who loves to talk) and my mother (my everything). Thank you mothers for your support and faith in me. I thank my uncle, Rajan and my aunt, Selvi for being my support even amidst challenging and tough circumstances. I thank all their family for taking me into their family and treating me as one of their own.

My love, my sweetheart, Roberto Marivela. Thank you for your immense support when I needed it and for your patience with all my eccentricities. Thank you for your faith in me and teaching me so many things.

Last but the most important of all: Thank you mother and father for giving me all the opportunities to explore the world. Every atom that I am is because of my mother, who was also a father to me. I cannot thank her enough for her guidance, faith, unconditional love and her belief in me. She gave more than what I needed to experience the world. I humbly bow down and surrender and celebrate my joys and victories with her.

Table of Contents

List of Figures

List of Tables

1. Introduction

Seafloor hydrothermal systems are an essential component of Earth's heat transfer regime, accounting for approximately 33% of the heat loss from the oceanic lithosphere [*Sclater et al.,* 1980; *Elderfield and Schultz,* 1996]. In addition, these complex circulation systems play an important role in cycling key chemical constituents [*Wolery and Sleep,* 1976; *Edmond et al.,* 1979; *Elderfield and Schultz,* 1996] and host an array of microbial and macrofaunal biological systems [*Jannasch,* 1983, 1985, 1995]. Because the seafloor hydrothermal environment exhibits sharp thermal and biogeochemical gradients, these environments have been proposed as a site for the origin of life [*Baross and Hoffman,* 1985] and have been used as analogues for the search for life on other planetary bodies in the solar system [*Nisbet and Sleep,* 2001; *Westall et al.,* 2013].

As a result of their importance, seafloor hydrothermal systems have been a focus of intense research for the past few decades [e.g., *Lowell et al.,* 2014]. Of particular interest are high temperature systems in young crust at oceanic spreading centers, where high-temperature fluids (~350 °C) laden with metal-rich particles discharge on the seafloor. These systems occur when cold seawater enters the permeable rocks, flows horizontally as it gets heated conductively near the top of the axial magma chamber, rises up through the rocks due to its thermally generated buoyancy, and finally discharges on the seafloor through chimney-like structures called vents. Metalliferous sediments and minerals precipitate when these hot fluids come in contact with the seawater [*Miller,* 1964, 1969; *Miller et al.,* 1966; *Degens and Ross,* 1969]. This circulation pattern is commonly referred to as the "single-pass" model because the fluid goes through the entire path once [*Elder,* 1965]; and it has often been used to model seafloor hydrothermal systems [e.g., *Lowell and Burnell,* 1991; *Lowell and Germanovich,* 2004; *Lowell et al.,* 2013].

One key issue that has yet to be resolved concerns fluid recharge patterns in high-temperature system at ocean ridges. In contrast to hydrothermal discharge, which is evidenced by high-temperature black smokers and low temperature diffuse flow sites, hydrothermal recharge areas are difficult to detect. The locations and circulation patterns of the recharge or source of these hot fluids in any hydrothermal system are largely unclear or being debated upon. Structural considerations suggest that recharge may be largely along axis as suggested by *Haymon et al.* [1991] for the East Pacific Rise (Figure 1).

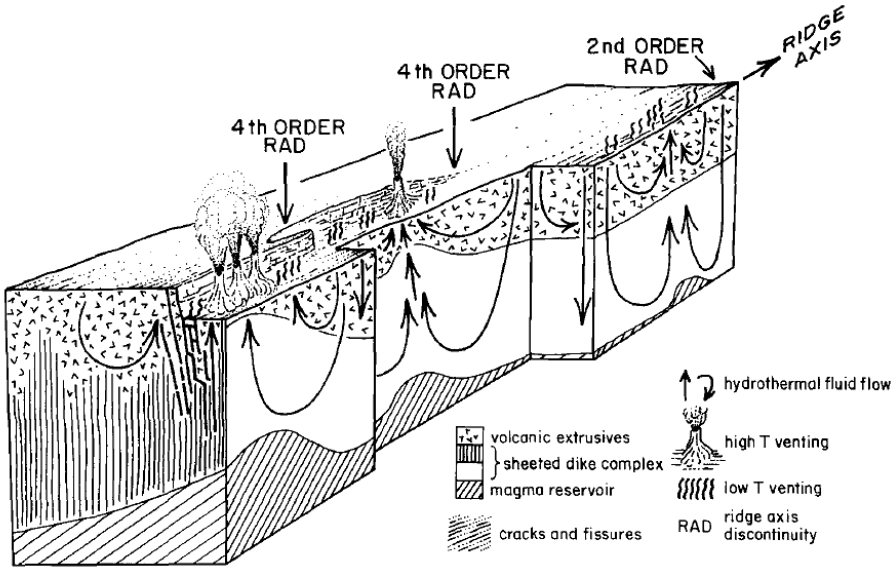

Figure 1. Schematic sketch of hydrothermal flow geometry proposed for a fast-spreading ridge crest, consistent with vent distribution observed in the Venture Hydrothermal Fields, EPR crest 9°09'- 54' N. This diagram represents an integrated model of ridge crest magmatic/tectonic activity and hydrothermal flow that includes the following features: (1) shallow 3-D circulation in the more permeable volcanics, superimposed on top of (2) 2-D ridge-parallel circulation in the relatively impermeable sheeted dike complex along cracked zones of enhanced permeability (3) along-axis segmentation of deep hydrothermal flow, due to (a) the spacing of recent magmatic intrusions (represented as bumps on the magma reservoir and on the upper bound of dike complex) and (b) lateral spatial shifts along-strike in zones of enhanced permeability in the dikes: (4) greater abundance of high T vents above shallower segments of the axial magma reservoir. This model emphasizes that the interaction between thermal and permeability fields governs hydrothermal flow at MOR crests. [from *Haymon et al.,* 1991].

Conversely, measurements of conductive heat flow using thermal blanket technology [*Johnson et. al.,* 2010] on the Juan de Fuca Ridge, suggest that recharge of the Main Endeavour field appear in a nested system of fluid circulation paths in the porous extrusive basalt (see Figure 2). In addition, local recharge may occur near high-temperature vents [*Johnson et. al.,* 2010], and numerical models indicate that deep recharge may occur near high temperature hydrothermal plumes [e.g., *Coumou et al*., 2008]. Also isotopic analysis of the vent fluids from the vent fields at Main Endeavour field show the presence of organic material leading *Lilley et al.* [1993] to suggest that the source of the organic material could be sediment ponds located along axis about 10 km away from the fields where the recharge zone may be possibly located.

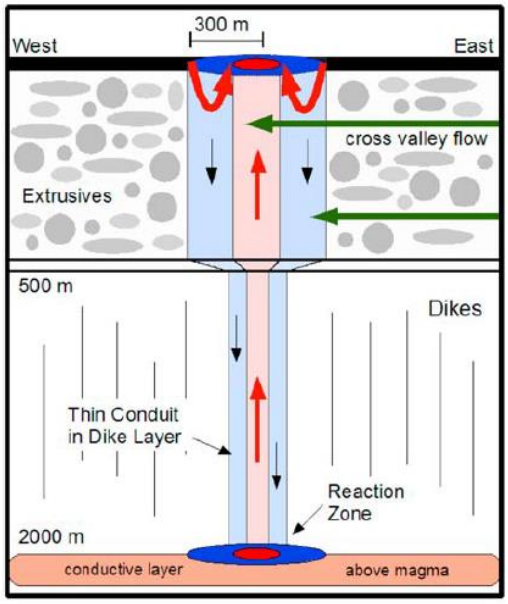

Figure 2. Cartoon of "nested" model of the subcrustal hydrothermal fluid circulation at MEF. Uppermost thick dark line represents the seafloor. Green horizontal arrows represent cross-valley flow, which can supply either the deeply sourced upwelling high-temperature fluid or the recharge fluid for the same system. Bright red arrows near the seafloor are the shallow circulation cells that feed the diffuse low-temperature venting adjacent to the large vent fields. [from *Johnson et. al.,* 2010]

Although hydrothermal recharge zones may be controlled in part by faults and high permeability fracture networks associated with dikes, other factors may impact recharge and its evolution as a function of time. It has long been recognized that as seawater enters the crust and is heated, $CaSO_4$ (anhydrite) will tend to precipitate and clog the recharge zone [*Mottl,* 1983; *Sleep,* 1991; *Lowell and Yao,* 2002]. On the other hand, seismicity may open new cracks and create or enhance local permeability [*Tolstoy et al.,* 2008]. Models of anhydrite precipitation during recharge using one dimensional models suggest that such mineral precipitation will rapidly clog the permeability of the recharge zone and thus lead to rapid decline of hydrothermal circulation [*Lowell and Yao,* 2002; *Lowell and Germanovich,* 2004; *Lowell et al.,* 2012] unless the area of recharge is much larger than the area of hydrothermal discharge. These one-dimensional models using the single-pass modeling approach may be over-restrictive, however, because they require all the fluid to pass through a thin zone in which the temperature gradient is high, and anhydrite precipitation is rapid.

Anhydrite precipitation may also occur in regions where cold, seawater mixes with hot hydrothermal fluid [*Lowell et al.,* 2003; *Pascoe and Cann,* 1995; *Fontaine et al.,* 2007]. In this case anhydrite precipitation may eventually inhibit mixing between cooler seawater and the upwelling hydrothermal plume [*Lowell et al.*, 2007]. This would result in the venting of fluids more reflective of conditions deep within the hydrothermal system.

In this paper, we construct a two-dimensional numerical model of hydrothermal circulation in a NaCl-H_2O fluid to better assess the rate of porosity and permeability reduction during anhydrite precipitation in a mid-ocean ridge hydrothermal system. The model focuses on the East Pacific Rise (EPR) hydrothermal system at 9°50'N for two reasons. First, a number of key data are available to constrain the numerical model; and secondly, seismicity data suggest that

the recharge zone for this system is small [*Tolstoy et al.,* 2008]. Consequently, the modeling performed here will either confirm the hypothesis of *Tolstoy et al*. [2008] or argue that recharge may be more complex than proposed.

In the next section, we describe the main features of the EPR 9°50'N hydrothermal system. Then we describe the numerical model, present the results and discuss the model implications.

2. EPR 9°50'N

The East Pacific Rise between 8° and 11° N is a fast spreading mid-ocean ridge with a full spreading rate of 11cm per year. It separates the Pacific plate from the North American, Riviera, Cocos, Nazca and Antarctic plates. The section of the ridge near 9°50'N was first studied intensively during a series of Alvin dives in April 1991 [*Haymon et al.,* 1993] following a visual and acoustic survey [*Haymon et al.,* 1991]. During this series of dives, it became apparent that a magmatic eruption had recently occurred; and to assess how hydrothermal activity and associated biota evolved following an eruption, the site became the focus of intense research as part of the RIDGE and RIDGE 2000 research programs. Another eruption in late 2005-early 2006 [*Tolstoy et al.*, 2006; *Soule et al.,* 2007] made this area one of the most magmatically active segments in the global mid-ocean ridge system. Consequently, the EPR 9°50'N hydrothermal system has become one of the best studied areas of the ridge system for providing a better understanding of the linkages between the dynamics of hydrothermal, biologic, magmatic, physical and chemical processes associated with the mid-ocean ridges. *Fornari et al.* [2012] provide a useful review of the past 20 plus years of research at EPR 9°50'N.

2.1. General Description

The EPR from 9°46'N to 9°56'N sits on an axial high at a depth of approximately 2500 m beneath the seafloor [*White et al.,* 2006; *Fornari et al.,* 2012; Figure 3].

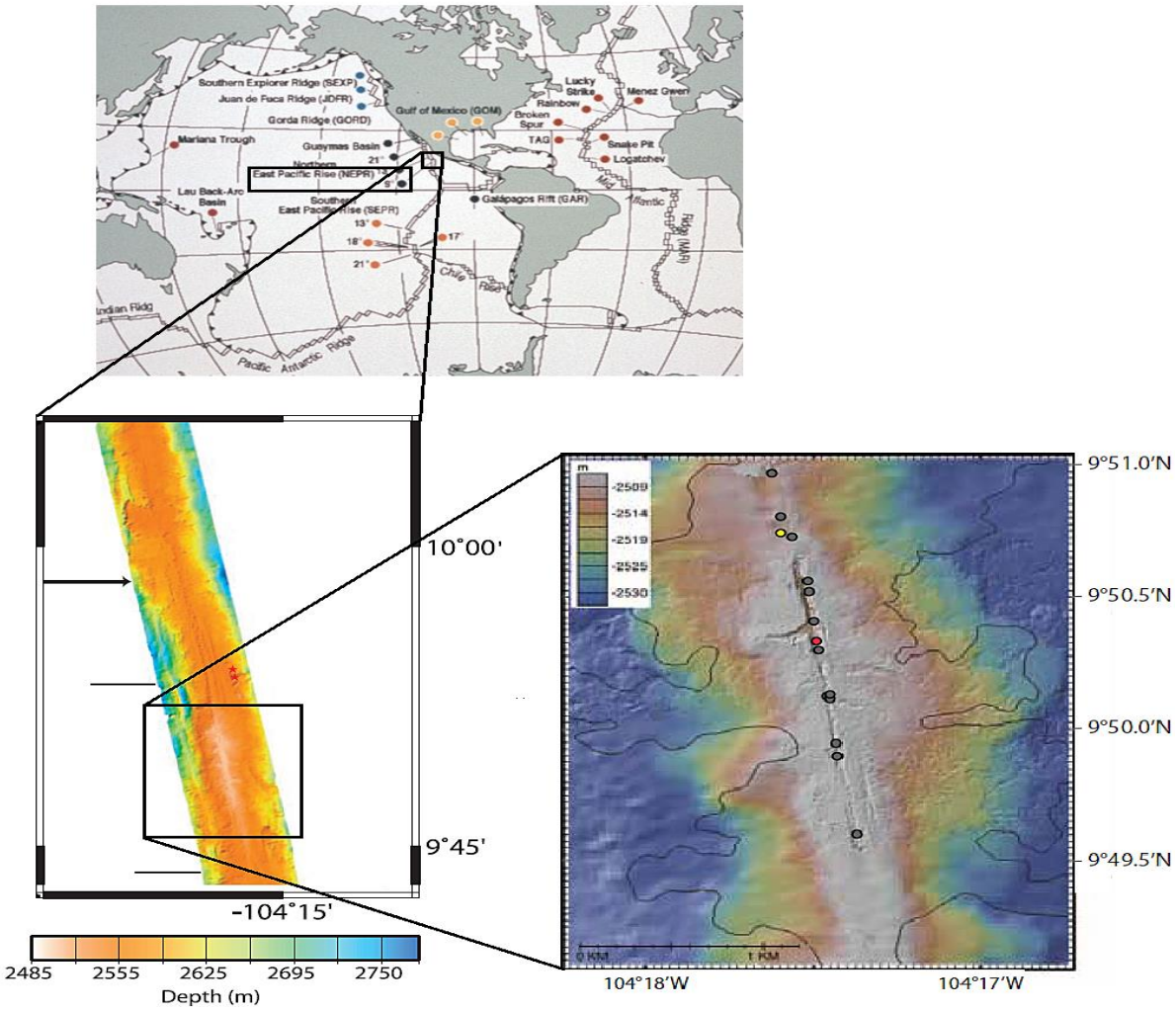

Figure 3. The figure at the top shows a partial distribution of the global mid-ocean ridge system. The East Pacific Rise is boxed in black which is then blown up in the bottom left figure. The boxed figure on the bottom left shows a shaded-relief bathymetric maps derived from 30m x 50m gridded EM300 depth measurements. Depth is plotted with a histogram-equalized color palette optimized for each panel to emphasize local changes in terrain. [Modified from *White et al.,* 2006]. The blown-up boxed figure on the bottom right shows bathymetric map of the EPR crest near 9°50'N made using 675 kHz scanning altimetric sonar on the autonomous underwater vehicle ABE (Autonomous Benthic Explorer) during cruise AT 7-4 on R/V Atlantis in 2001 [*Fornari et al.,* 2004]. The dots represent the vent sites with the yellow dot showing the Q vent and the red dot showing the Bio 9 vent. [from *Fornari et al.,* 2012].

A number of closely-spaced high-temperature vents are located along this axial high in an ~ 2 km zone extending from approximately 9°49'N to 9°51'N (see Figure 4). The vents tend to occur in a relatively narrow region near the axial summit trough, resulting in a vent field area of approximately 10^4 m^2 [*Lowell et al.,* 2013]. The vents can be broadly divided into a "Northern" and "Southern" group. The Northern group starts with the Biovent near 9°51'N and extends to just north of Bio9'. The other high-temperature vents in this group are M, Q and Tica vents. The Southern group starts with Bio9, Bio9', and P and extends to Tube Worm Pillar (TWP) to the south. The other high-temperature vents of this group are Ty and Io. (see Figure 4).

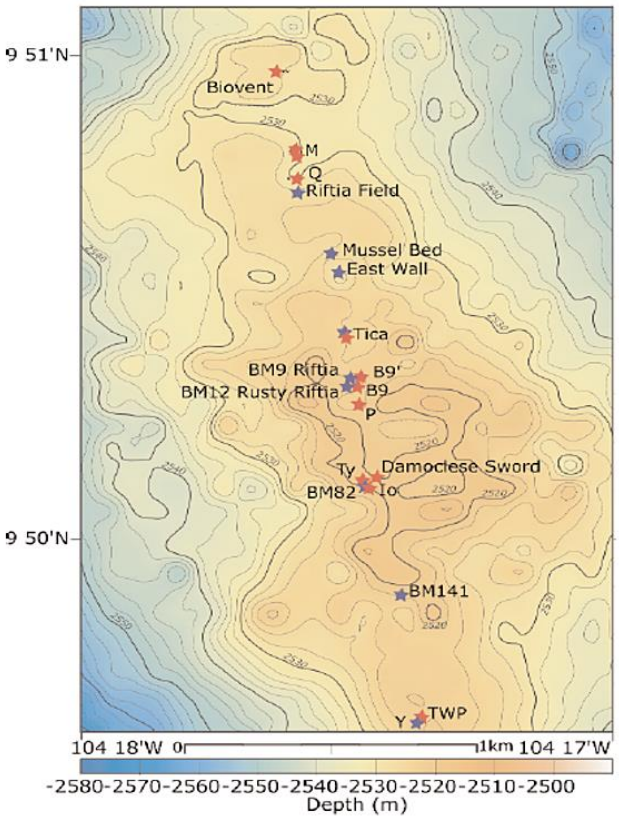

Figure 4. Location of all high- (red stars) and low-temperature (blue stars) hydrothermal vents along the EPR axis between 9°49'N to 9°51'N. [from *Fornari et al.*, 2004].

2.2. Observational Constraints

Temperature and salinity of the high-temperature vents at EPR 9°50'N have been measured on a number of cruises since 1991. Figure 5 shows the most complete data, which are from Bio 9, Bio9' and P vent. These data show that vent temperatures have fluctuated about a mean of approximately 370 °C and that the vent salinity is generally less than seawater, indicating phase separation must occur at some depth beneath the seafloor.

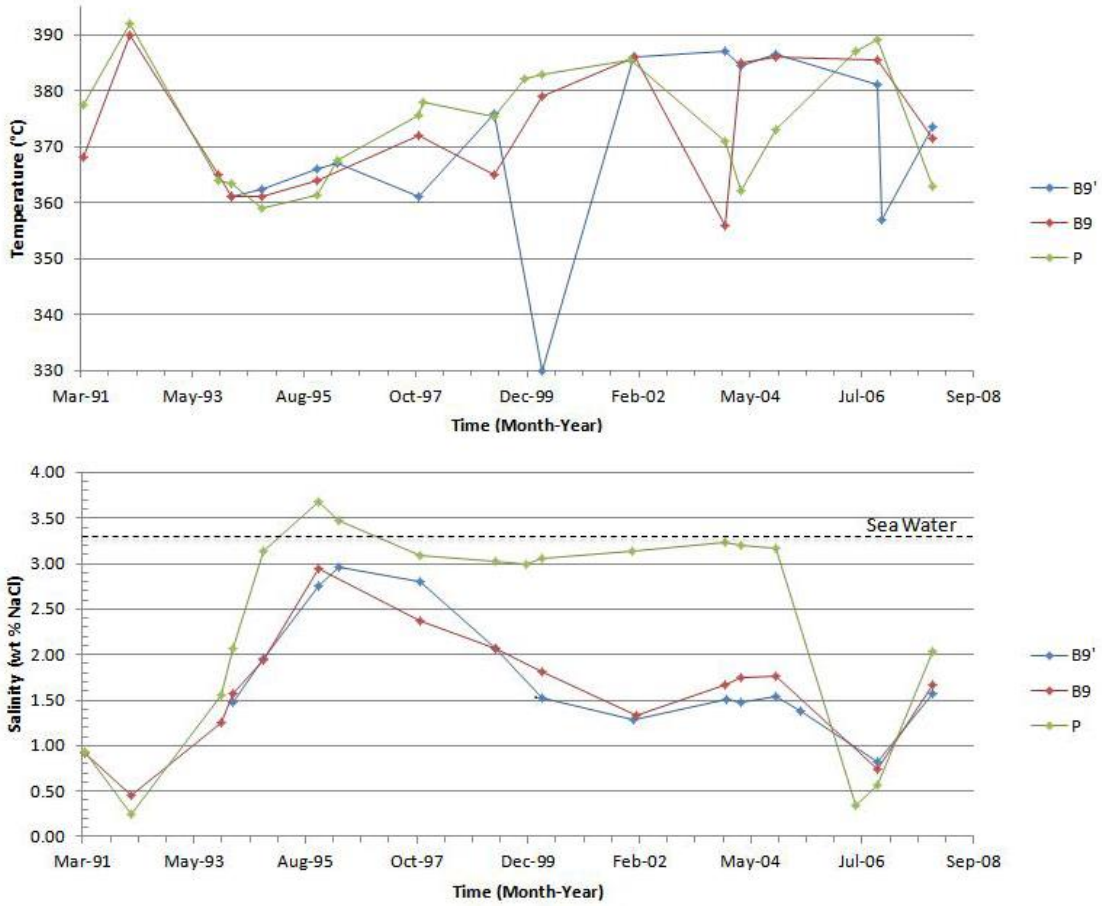

Figure 5. Discrete measurements of (a) temperature and (b) salinity at Bio9, Bio9' and P vents at EPR 9°50′ N between 1991 and 2008, spanning two eruptive events in 1991-1992 and 2005-2006. (from compilation of N. EPR vent fluid temperature, chloride, pH and Min. Mg values K.L. Von Damm, J.G. Bryce, and M.F. Prado, MGDS database) [from *Choi and Lowell*, 2015]

Ramondenc et al. [2006], estimated the heat output of the EPR 9°50'N hydrothermal system from a number of point measurements of high-temperature vents and a single measurement on a patch of diffuse flow. By extrapolation they estimated the heat output from Biovent to TWP to be 325 MW +/- 160 MW. The heat output appears to be evenly divided between the Northern and Southern vents and approximately 90% of the heat output appears as diffuse flow.

A seismic reflection survey [*Detrick et al.,* 1987] detected a thin ribbon-like layer of melt present nearly continuously beneath the ridge axis between 9° 03'N and ~ 10° N. This melt layer, called the Axial Magma Chamber (AMC), lies at a depth ranging between 1.2 km and 2.4 km, has an across-axis width of ~ 0.1 km and a thickness ~ 10-50 m [*Kent et al.,* 1993]. Near 9°50'N its depth is ~ 1.5 km beneath the seafloor, but it may fluctuate by +/- 90 m. A repeat 3D seismic reflection survey [*Carbotte et al.,* 2013] suggests that the magma lens is uninterrupted between 9°48'N and 9°51'30"N; however there is a 4th order discontinuity (slight deviation in axial linearity; *Macdonald et al.*, 1991) near 9°49.25′ [*Carbotte et al.,* 2013; Figure 6]. The AMC, which appears to undergo relatively frequent episodes of replenishment [*Soule et al.,* 2007; *Goss et al., 2*010] and perhaps non-eruptive diking events [*Germanovich et al.,* 2011] supplies the heat that drives the 9°50'N hydrothermal vents.

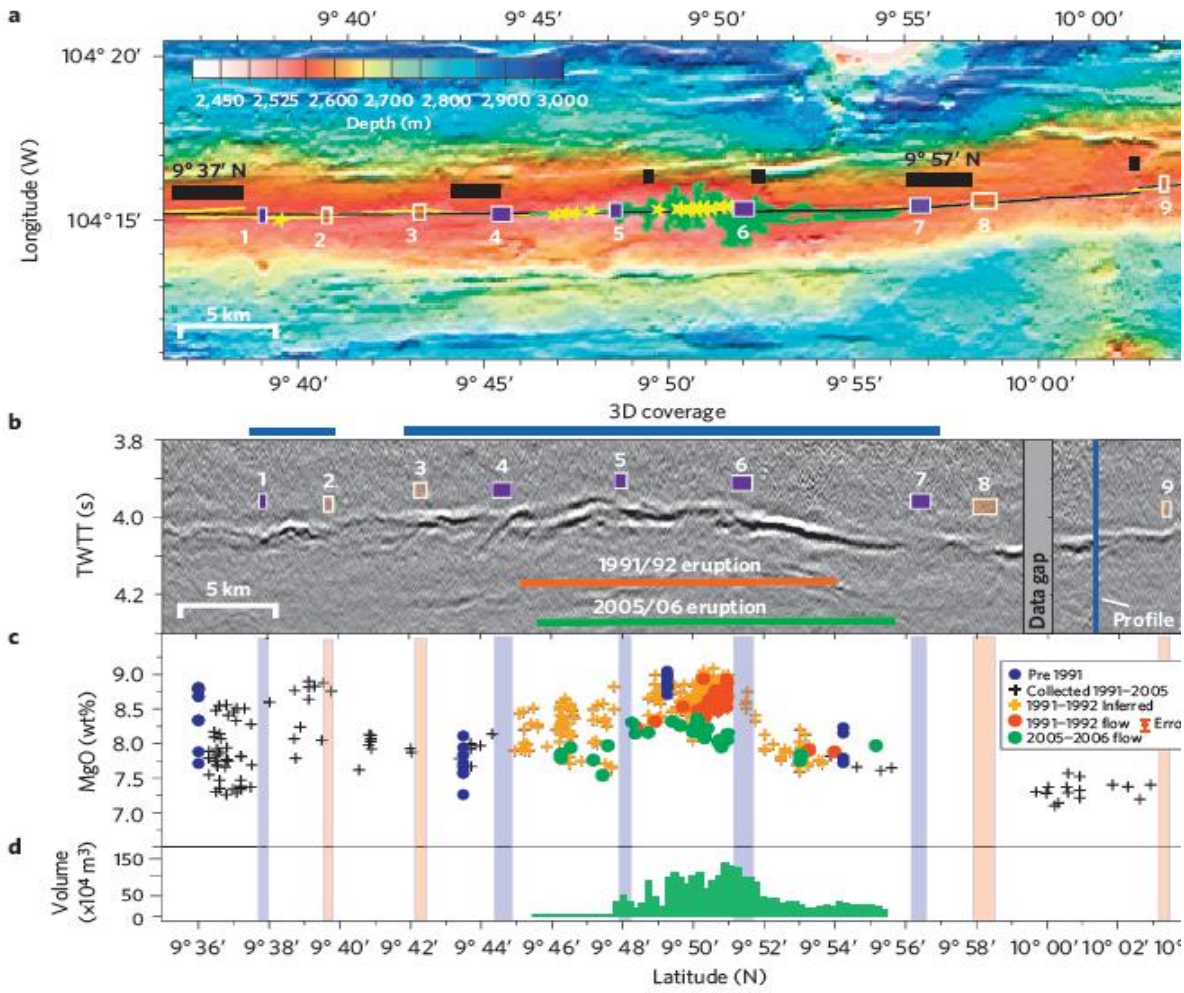

Figure 6. Segmentation in seafloor structure, Axial Magma Lens, lava geochemistry and eruption volume along the EPR 9°35'–10°06'N. a. Bathymetry showing location of axial eruptive zone (yellow line) and composite axial seismic profile (black). Black rectangles: third- (labelled) and fourth-order tectonic discontinuities. Yellow stars: hydrothermal vents; green region: 2005–2006 lava flow. b. Composite axial seismic reflection section (stacked) showing magma lens reflection and interpreted disruptions. TWTT, two-way travel time. Numbered rectangles in a,b indicate magma lens disruptions identified from seismic data (purple, data from 3D seismic volume). c. MgO composition of seafloor lavas located within 500m of the axis colour-coded for eruption period. d. Volume of erupted 2005–2006 lavas. Vertical bars (translucent purple and orange) mark magma lens disruptions from a,b. Note the absence of disruptions between 9°48'N and 9°51'30"N. [from *Carbotte et al.,* 2013]. Reprinted with permission from Nature Geoscience: Carbotte, S.M., M. Marjanovic, H. Carton, J.C. Mutter, J.P. Canales, M.R. Nedimovic, S. Han, and M.R. Perfit, doi: 10.1038/NGEO1933, copyright (2013)

2.3 Seismicity and Hydrothermal Recharge

A nine two-component OBS array recorded >7,300 microearthquakes at the EPR 9°50'N between October 2003 and April 2004 [*Tolstoy et al.*, 2008; see Figure 7]. Some of the earthquakes, which are interpreted to be due to tectonic stresses, were located in a vertical narrow pipe-like zone near a 4th-order axial discontinuity at ~9° 49.25'N. Other earthquakes occurred in a horizontal band-like formation, around 500m thick, just below the vertical cluster and right above the AMC. This band could be the area of hydrothermal cracking where down-welling seawater get heated. The occurrence of less dense cloud of hypocenters right above Ty, Io and P vents is because of the high T fluid upflow (see Figure 8). All these observations lead to the hypothesis that the circulation is focused along-axis and that the vertical zone of hypocenters

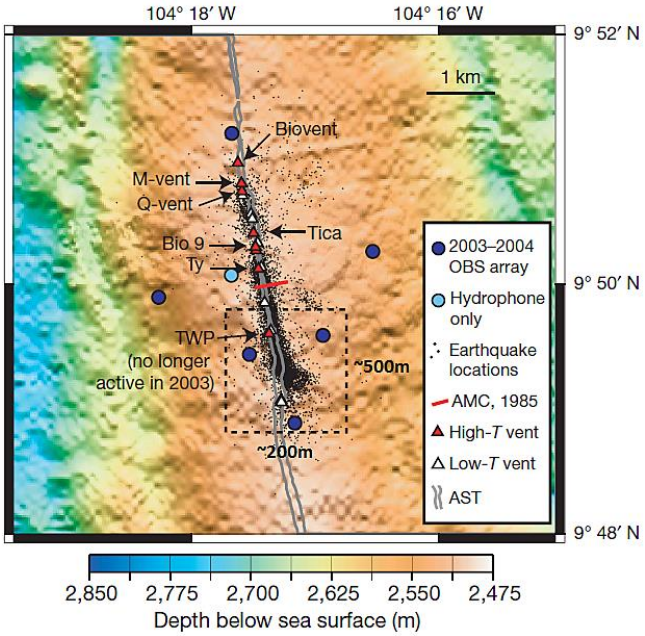

Figure 7. Bathymetric site map showing earthquake epicentres (black dots) within the OBS array (blue circles). Dashed box outlines recharge area. [from *Tolstoy et al.,* 2008]. Reprinted with permission from Nature Geoscience: Tolstoy, M., F. Waldhauser, D.R. Bohnenstiehl, R.T. Weekly, and W.-Y. Kim, doi: 10.1038/nature06424, copyright (2008).

depicts the recharge zone for the southern group of hydrothermal vents at EPR 9°50'N. The area of approximately 500m by 200m (see Figure 7), delineates a relatively focused region of hydrothermal recharge [*Tolstoy et al.*, 2008]. Figure 8 shows the circulation pathways proposed by *Tolstoy et al.* [2008], which also suggests that the northern and southern hydrothermal vents are part of two separate circulation cells.

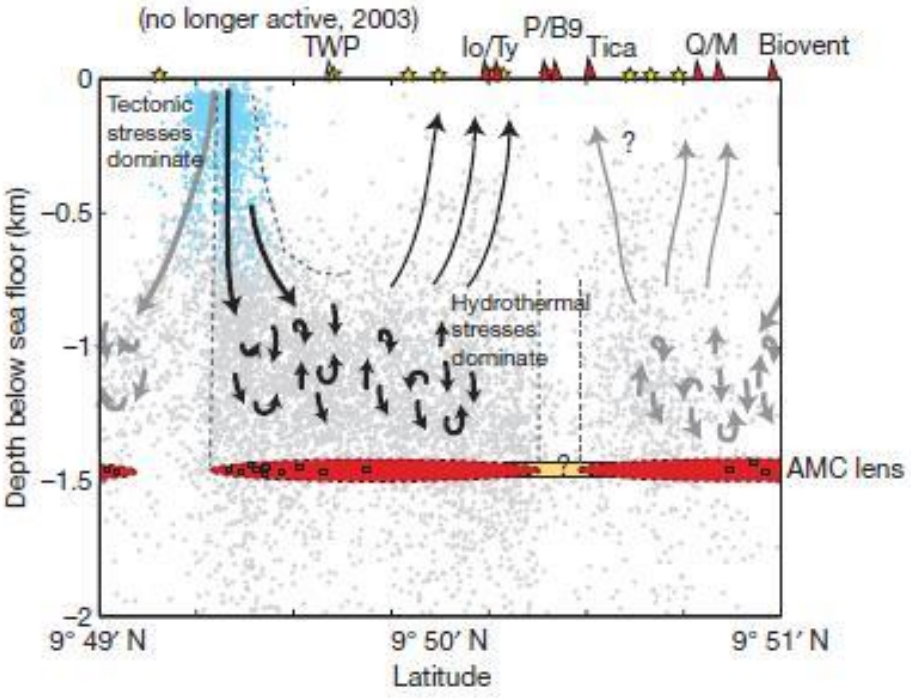

Figure 8. Cartoon illustrating hydrothermal cell structure. The blue dots represent the vertical pipe-like zone of earthquakes by tectonic stresses. The cluster of grey dots represent the horizontal band of seismicity due to hydrothermal stresses. The very less dense cloud of hypocenters below Ty and Io can also be seen here. TWP and Biovent, the closest vents to the inferred down-flow zones, both show decreases in temperature with time, whereas the central vents have been steadily increasing in temperature since about 1994. [from *Tolstoy et al.,* 2008]. Reprinted with permission from Nature Geoscience: Tolstoy, M., F. Waldhauser, D.R. Bohnenstiehl, R.T. Weekly, and W.-Y. Kim, doi: 10.1038/nature06424, copyright (2008).

Tolstoy et al. [2008] also argue that the lack of seismicity under TWP and also it's rapid decline in vent temperature leading to its inactivity in 2003 supports this interpretation for the

location of the recharge zone. They recognize that *Lowell and Yao* [2002] argued that the permeability of such a narrow recharge zone would clog rapidly due to anhydrite precipitation, but counter that the tectonic and hydrothermal stresses indicated by the high level of seismicity could open up new fractures thereby maintaining permeability.

Table 1. Observational data at EPR 9°50'N used in 2D numerical modeling[1]

Observational Parameter	**Value**
Vent field length	~1.5 km
Vent field area	1.0E+04 m^2
Depth to magma chamber	~1.5 km
AMC area	1.0E+06 m^2
Mean vent temperature	371 °C
Measured heat output	160 MW

[1] The values in Table 1 assume the circulation pattern for just the southern vents as suggest by *Tolstoy et al.* [2008] and not the full system suggested by the more recent seismic data of *Carbotte et al.* [2013].

To test the hypothesis of *Tolstoy et al.* [2008] that hydrothermal recharge at EPR 9°50'N occurs in a relatively small area and that circulation is primarily along axis, we construct 2D numerical models of two-phase flow in a permeable medium using the numerical simulator FISHES [*Lewis et al.,* 2009a,b]. Table 1 shows the key observational data that constrains the model. We note that a simple single-pass modeling approach [*Lowell et al.,* 2013] using values of measured heat output, mean vent temperature, AMC area, and vent field area provide constraints on mass flow rate (Q), mean permeability of the hydrothermal discharge zone (k_d), and thickness of the conductive boundary layer (δ) between the AMC and the base of the hydrothermal system. From *Lowell et al.* [2013], Q ~ 86 kg/s, $k_d \sim 3 \times 10^{-13}$ m^2 and δ ~13 m.

3. Mathematical Formulation for EPR 9°50'N Circulation Models

3.1. FISHES – A Numerical Code

FISHES code combines a finite volume equation solver [*Patankar,* 1980] with the equations of state for a NaCl-H_2O solution composed of thermodynamic lookup tables. *Faust and Mercer* [1979] gives the equations that govern the conservation of mass, momentum and energy in the NaCl-H_2O system. The mass continuity equation is

$$\frac{\partial(\phi\rho)}{\partial t} + \nabla \cdot (\rho_v \overrightarrow{v_v} + \rho_l \overrightarrow{v_l}) = 0 \quad [1]$$

where ϕ is the porosity, ρ is the bulk density, v is the Darcian velocity and the subscripts v and l refer to vapor and liquid phases respectively. The momentum conservation equations are

$$\overrightarrow{v_v} = -\frac{k k_{rv}}{\mu_v}(\nabla P - \rho_v g \nabla z) \quad [2]$$

$$\overrightarrow{v_l} = -\frac{k k_{rl}}{\mu_l}(\nabla P - \rho_l g \nabla z) \quad [3]$$

where k is the permeability, k_r is the relative permeability, P is the pressure, z is the depth, μ is the dynamic viscosity and g is the gravitational acceleration. The energy conservation is given by

$$\frac{\partial}{\partial t}[\phi\rho h + (1-\phi)\rho_r c_r T] + \nabla \cdot (\rho_v h_v \overrightarrow{v_v} + \rho_l h_l \overrightarrow{v_l}) = \nabla \cdot (\lambda_m \nabla T) \quad [4]$$

where h is the specific enthalpy, T is the temperature, λ_m is the effective medium thermal conductivity and the subscript r refers to the rock; ρ and h without subscripts refer to bulk quantities.

The salt conservation equation is given by [*Bai et al.,* 2003]

$$\frac{\partial}{\partial t}(\phi\rho X) + \nabla \cdot (\rho_v X_v \overrightarrow{v_v} + \rho_l X_l \overrightarrow{v_l}) = \nabla \cdot (\phi\rho_v D \nabla X_v + \phi\rho_l D \nabla X_l) \quad [5]$$

where X is the bulk salinity and D is the salt chemical diffusivity.

As the system consists of two components, three independent variables are needed to characterize the state of the system. Pressure (P), Temperature (T) and Bulk Salinity (X) are chosen as the three primary variables and the derived equations from these variables are solved in FISHES using a fully implicit finite volume method. P, T, and X are solved at the centroid of each control volume. *Lewis* [2007] gives detailed derivations of the discretized equations. The code FISHES is available for download at http://wlb-physics-01.monmouth.edu/fishes.htm and its manual is available for download at http://www.geophys.geos.vt.edu/rlowell/kaylal/FishMan-1.0.pdf

FISHES uses the finite volume method patterned after *Patankar* [1980] where initially the domain is partitioned into a grid of control volumes (see Figure 9). The next step is to integrate

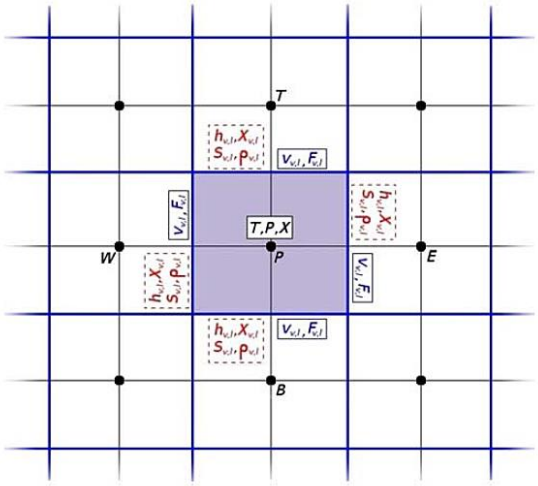

Figure 9. A magnified portion of an example space discretization, with a shaded internal control volume. Nodes labels are as follows: P refers to the position of the current node; W, E, T, and B refer to the nodes immediately westward, eastward, upward, and downward, respectively. The primary variables (T, P, and X) are calculated at the shaded control volume node, while fluid velocities (v_v, v_l), salt, mass, and energy fluxes (collectively labeled as F_v, F_l) are calculated at the control volume boundaries. Upstream weighting is applied to the variables in dashed boxes. [*Lewis et al.,* 2009a]

the governing equations over the control volume for a time step Δt. Then approximations are made that result in a system of linear equations where the primary variables (P, T, X) at each centroid is a function of those at the adjacent centroids. Finally, the set of linear equations are solved subject to time step and grid size constraints. Figure 10 shows a schematic of the algorithm discussed above.

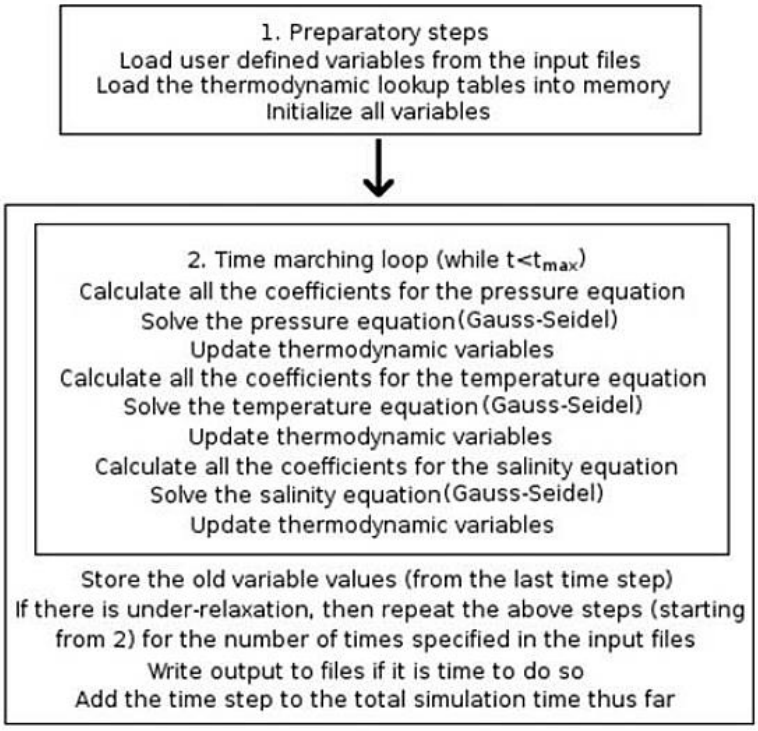

Figure 10. Schematic outline of the main algorithm for FISHES. [from *Lewis et al.,* 2009a]

3.2. Parameters and Model Geometry

Based on the vent field scale parameters in Table 1, we construct a square 2D box with dimensions 1500m across and 1500m deep. The temperature at the top of the system is kept at 10ºC to approximate the temperature of the seawater that enters the oceanic crust. The salinity is initially at 3.2wt% NaCl-H_2O solution to approximate seawater salinity [*Bischoff and Rosenbauer,* 1984]. The pressure at the top of the system/seafloor is maintained at 25MPa and

the initial pressures increase hydrostatically with depth [*Lewis and Lowell,* 2009a]. The initial porosity is taken as 0.1 (10%). For models with homogeneous permeability we use $k = 10^{-13}$ m^2; when layer 2A is included we assume its permeability is 10^{-12} m^2 (see Figure 11). These values give reasonable agreement with the results of the single pass model [*Lowell et al.,* 2013; Table 1].

As a basic model for EPR 9°50'N, we consider a central-heated model with a 25 m cell size. We assume that the temperature at the bottom of the system increases uniformly from 300 °C ($T_{bot\ min}$) at each end of the box to 450 °C over a distance of 250 m and is maintained at 450 °C ($T_{bot\ max}$) for the 1000m in the center of the box, to correspond to the axial magma chamber. The maximum bottom temperature ensures that phase separation occurs near the base of the heated zone [*Han et al.,* 2013]. Using an isothermal basal boundary condition simplifies the physics of the hydrothermal system, which is driven by heat transfer from a convecting, crystallizing, replenished magma sill [e.g., *Liu and Lowell,* 2009]. Such a boundary condition would potentially result in complex spatially and temporally varying temperature and flow conditions in the model, however. Since a primary goal of this work is to estimate how porosity and permeability change results from anhydrite precipitation, and to compare the numerical results with the 1D analytical model, we believe the more complex basal boundary condition is unwarranted for these simulations. Figure 11a shows the model geometry. Figure 11b shows the system with a 200 m thick layer 2A included.

The lower temperature regions near the edges of the box correspond to the recharge zone proposed by *Tolstoy et al.* [2008]. This simulation assumes that the circulation pattern between approximately 9°48'N and 9°51'N consists of two separate cells as proposed by *Tolstoy et al.*

[2008] [see Figure 8]. This model thus simulates the southern group of vents between TWP and Bio 9 [Figures 7 and 8].

Although the plume structure and temperature is generally established after approximately 50 years, model simulations are run for 100 years to simulate the EPR 9°50'N vent temperature and salinity. The resulting temperature and velocity fields at 50 and 100 years are used to characterize anhydrite precipitation. Anhydrite precipitation is assumed to occur by precipitation of $CaSO_4$ from seawater in the temperature range between 150° and 250° C. We assume that the rate of anhydrite precipitation is controlled by the "gradient reaction" [e.g., *Phillips*, 1991] as fluid moves across the temperature gradient and the solubility of $CaSO_4$ decreases as temperature increases. We then calculate the rate of porosity and permeability reduction in a given cell as anhydrite precipitates. Consequently, the simulation results yield the locations of anhydrite precipitation, and enable one to estimate rates of change in porosity and permeability and potential sealing times of those zones at a two snapshots in time. The methodology is discussed in the next section.

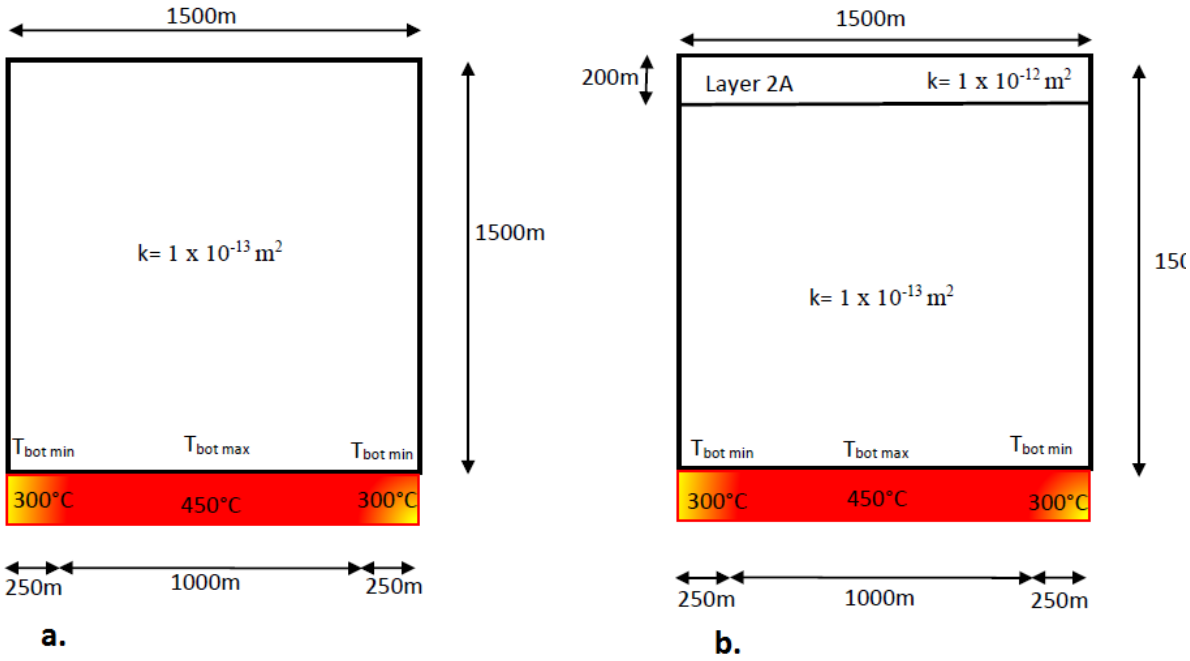

Figure 11. Schematic representation of the central-heated model. a. Model without layer 2A; b. Model with layer 2A

4. Anhydrite Precipitation and Evolution of Porosity and Permeability

The change in porosity as a function of time is expressed through a simple mass balance expression relating the change in pore volume to the rate at which concentration of anhydrite in the fluid changes along the flow direction [*Lowell et al.*, 1993]. Experiments have shown that solubility of anhydrite decreases as temperature increases and the main zone of precipitation occurs between ~150 °C and ~250 °C [*Bischoff and Seyfried*, 1978; Figure 12a].

Seawater contains approximately 10 mmol/kg Ca and 30 mmol/kg SO_4; so as precipitation occurs, a considerable amount of sulfate still remains when all the Ca is removed from seawater. As seawater reacts with basalt within the above-mentioned range of temperatures, Mg^{2+} in seawater is removed and Ca^{2+} is released to the solution [e.g., *Bischoff and Dickson*, 1975; *Seyfried and Bischoff*, 1981]. Consequently the amount of anhydrite precipitated may be greater than accounted for by the direct heating of seawater. Some sulfate may precipitate as $MgSO_4$

[*Bischoff and Seyfried*, 1978], and some seawater sulfate is reduced to sulfide [e.g., *Shanks et al.*, 1995]. Hence the amount of anhydrite that precipitates as seawater is heated and water-rock reactions occur is somewhat uncertain. Here we use the data from *Bischoff and Seyfried* [1978] for the precipitation of anhydrite from seawater as a function of temperature, recognizing that this may be an underestimate of the total amount of anhydrite precipitated during recharge and as heated seawater mixes with rising hydrothermal plumes.

Assuming that anhydrite precipitation occurs only as a result of heating seawater, the change in porosity as a function of time is expressed through a simple mass balance expression relating the change in pore volume to the rate at which concentration of anhydrite C in the fluid changes along the flow direction [*Phillips,* 1991]. This is given by,

$$\boldsymbol{\rho_{an}}\ \frac{\boldsymbol{d(\emptyset/\emptyset_0)}}{\boldsymbol{dt}} = \frac{\boldsymbol{\rho_f}}{\boldsymbol{\emptyset_0}}\ \vec{\boldsymbol{u}}.\boldsymbol{\nabla C(P,T)} \qquad [6]$$

where ρ_{an} and ρ_f are the densities of the precipitating mineral, anhydrite, and fluid respectively, $\frac{\boldsymbol{dC_{eq}}}{\boldsymbol{dT}}$ is the solubility of anhydrite as a function of temperature and $\boldsymbol{\emptyset_0}$ is the initial porosity. Equation [6] assumes that dispersion can be neglected relative to advection and anhydrite precipitation can be written as a "gradient reaction" where the rate of precipitation is governed by mineral solubility as the fluid moves along temperature and pressure gradients [Phillips, 1991]. As the pressure dependence of anhydrite solubility is much smaller than its dependence on temperature [*Blounot and Dickson*, 1969] the pressure term is neglected. We also neglect kinetic effects and assume that the rate of precipitation is controlled by the solubility as a function of temperature Neglecting the pressure term and applying the chain rule, equation [6] becomes,

$$\frac{\boldsymbol{d(\emptyset/\emptyset_0)}}{\boldsymbol{dt}} = \frac{\boldsymbol{\rho_f}}{\boldsymbol{\rho_{an}\emptyset_0}}\ \frac{\boldsymbol{dC_{eq}}}{\boldsymbol{dT}}\left[\boldsymbol{u_x}\frac{\boldsymbol{dT}}{\boldsymbol{dx}} + \boldsymbol{u_z}\frac{\boldsymbol{dT}}{\boldsymbol{dz}}\right] \qquad [7]$$

where u_x and u_z are the Darcian velocities in the x and z directions, respectively and $\frac{dT}{dx}$ and $\frac{dT}{dz}$ are the temperature gradients in the x and z directions, respectively.

Experimental results for the solubility of anhydrite in seawater at P = 500 bars is shown in Figure 12a. This shows data at 50°C increments between 150 and 350°C [*Bischoff and Seyfried,* 1978] and are fit by a smoothed curve [*Lowell and Yao*, 2002]. The smoothed derivative which is then derived from this data averaged over 5°C intervals between 150 and 350 °C is shown in Figure 12b. It is observed from the figure that the highest rate of decrease in solubility occurs between 150 and 200°C, with the rate of solubility nearly vanishing above 250 °C [*Lowell and Yao*, 2002].

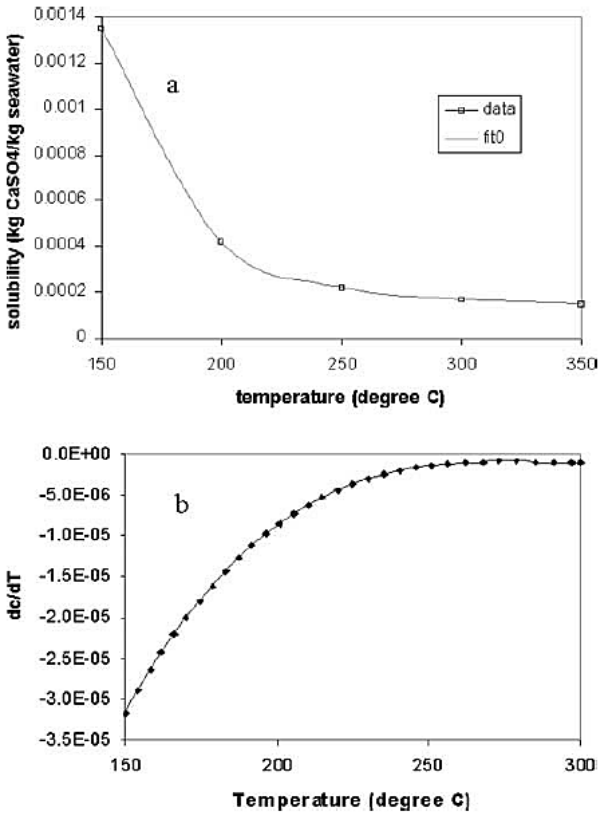

Figure 12. (a) Solubility of anhydrite as a function of temperature determined from *Bischoff and Seyfried* [1978]. (b) The derivative of the solubility as a function of temperature derived from the fit to the data of *Bischoff and Seyfried* [1978]. [from *Lowell and Yao,* 2002].

To calculate the rate of porosity reduction resulting from anhydrite precipitation at a simulation time of 50 years and 100 years, we first identified the cells with temperatures ranging from 150-250°C. We then interpolated the values of $\frac{dC_{eq}}{dT}$ from Figure 12b. Using the temperature distribution from the FISHES simulation, temperature gradients, $\frac{dT}{dx}$ and $\frac{dT}{dz}$ were calculated along with the liquid velocities u_x and u_z. Bulk density distribution from FISHES was taken for ρ_f, the density of the fluid. The density of anhydrite ρ_{an} was taken as 3000 kg m^{-3} [*Robie et al*., 1966] and $\emptyset_0$ was assumed to be 0.1. These values were then input into equation [7] to calculate $\frac{d(\emptyset/\emptyset_0)}{dt}$. The time τ taken to seal a given cell completely is then given by,

$$\boldsymbol{\tau = \frac{1}{\frac{d(\emptyset/\emptyset_0)}{dt}}} \quad [8]$$

In addition we assume that porosity and permeability can be related through a cubic law [*Bear*, 1972],

$$k = k_0[\emptyset/\emptyset_0]^3 \quad [9]$$

Equation [9] shows that if the porosity is just reduced by half, the reduction in permeability is almost one order of magnitude.

5. Results

5.1 Hydrothermal flow patterns and temperature evolution

The temperature distributions at 50 and 100 years for the central-heated model are shown in Figure 13c and d. The plume distribution is symmetric about the center of the system. The two plumes that reach the surface at around 400 m and 1100 m distance are stable plumes that started developing at about 10 years (see Figure 13a) and reached the surface at 18 years (see Figure 13b). They have maintained almost the same location for the rest of the simulation run time. At 50 years (see Figure 13c), the temperature of the plumes is ~338 °C and their salinity is ~3.27 wt%. At 100 years, the vent temperature of the two plumes is ~305 °C and their salinity is ~3.24 wt%. The cooling of the plumes during that time period results because the focused recharge that occurs along the sides of the adjacent plumes takes time to fully develop and eventually cools the plumes. The plume in the center develops at ~15 years, reaches to 400m below seafloor at 60 years and stays in the same place till 100 years.

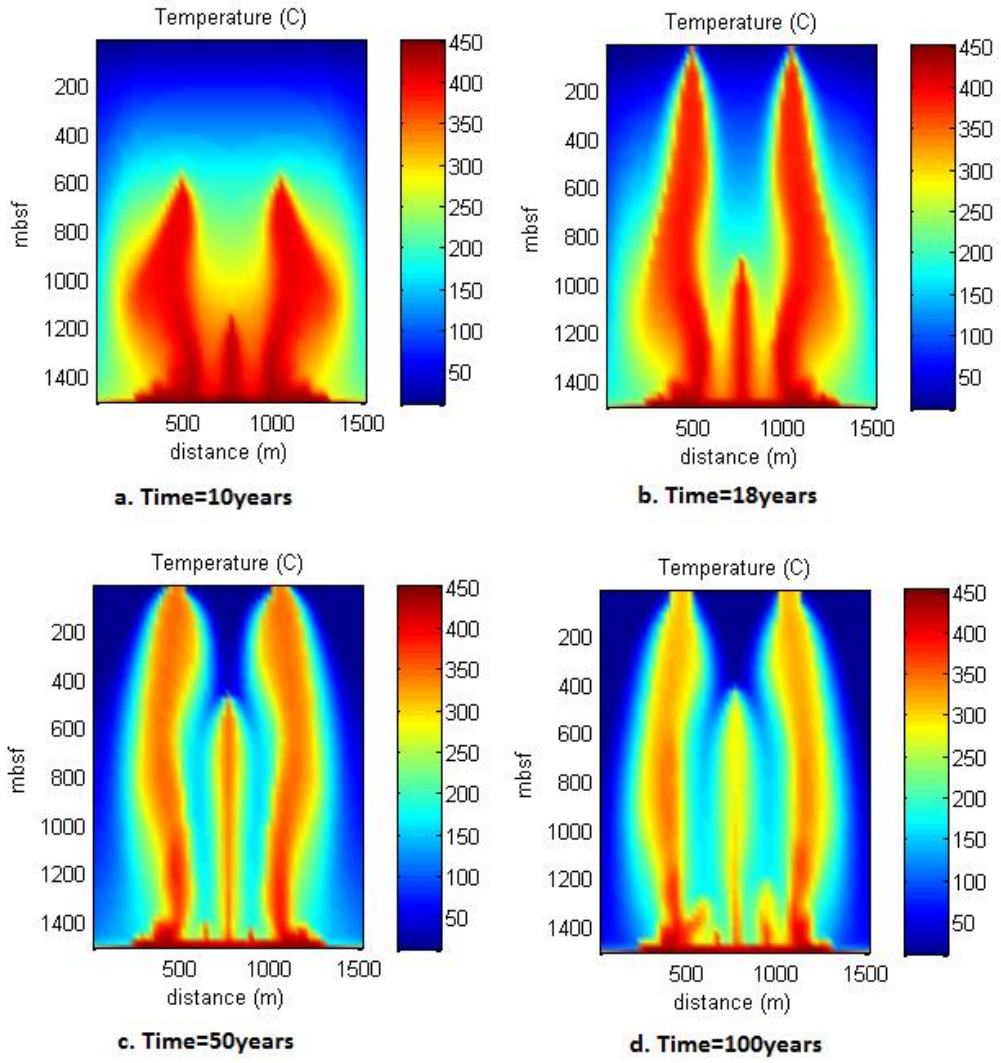

Figure 13. Temperature distribution plot for central-heated model at a. Time = 10years, b. Time = 18years, c. Time = 50years, d. Time = 100years

The temperature distributions at 50 years for the central-heated model with layer 2A is shown in Figure 14d. The plume distribution is symmetric about the center of the system. The two plumes that reach the surface at around 400 m and 1100 m distance are stable plumes that started developing at about 8 years (see Figure 14a) and reached the surface at 16 years (see Figure 14b). They have maintained almost the same location for the rest of the simulation run time. At 25 years (see Figure 14c), the temperature of the plumes is ~240 °C and their salinity is ~3.17

wt%. At 50 years, the vent temperature of the two plumes is ~204 °C and their salinity is ~3.21 wt%. As in the simulation without layer 2A, cooling of the plumes during that time period occurs because the focused recharge near the sides of the plumes takes time to fully develop and eventually cool the plumes. Also note that the temperature in the vents for this model with layer 2A is much lower than in the model without layer 2A. This is because the high permeability layer 2A facilitates shallow recharge that mixes with the hot fluids and cools them considerably before they vent. The plume in the center develops at ~15 years, reaches to 500m below seafloor at 50 years.

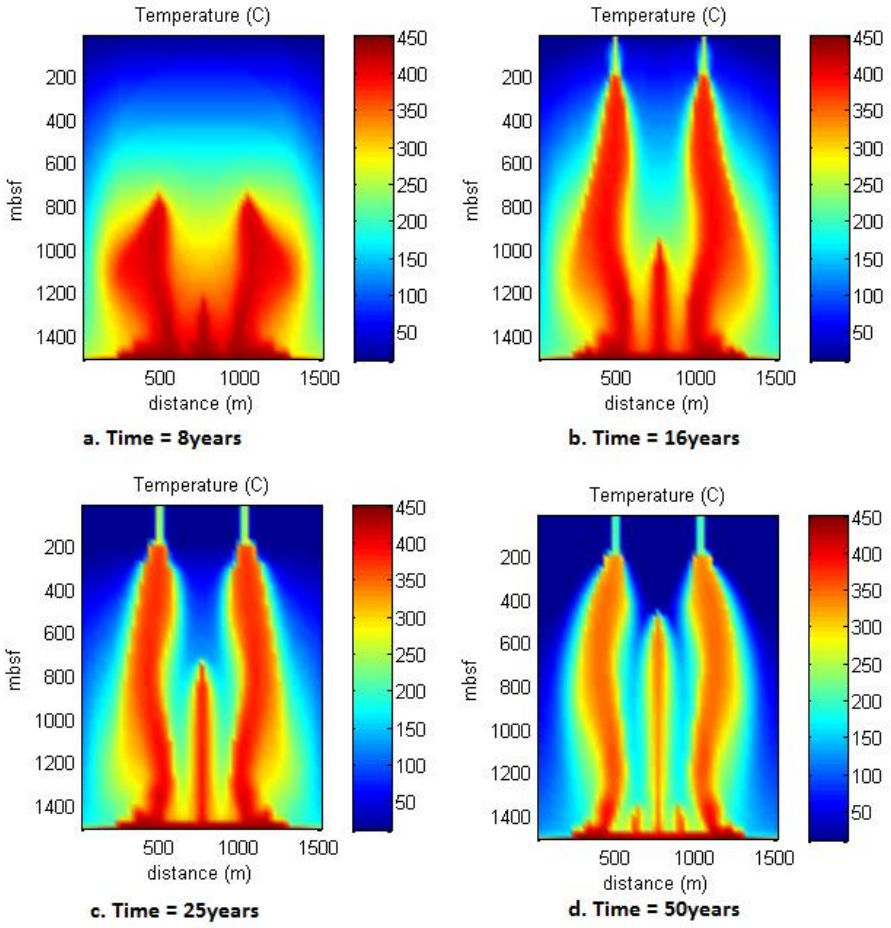

Figure 14. Temperature distribution plot for central-heated model with layer 2A at a. Time = 8 years, b. Time = 16 years, c. Time = 25 years, d. Time = 50 years

5.2. Zones of Anhydrite Precipitation

The methodology to obtain sealing times and rate of change of porosity with time as explained in section 4 was implemented in the results from the two FISHES models at 50 and 100 years for the central-heated model and at 50 years for the central-heated model with layer 2A.

For the central-heated model, Figures 15 and 16 show that regions of anhydrite precipitation lie along the sides of the two symmetrical plumes and along the middle plume. The isotherms of temperature distribution of the system at 50 and 100years are shown in Figure 15a and b. At 50 and 100 years, the areas with the fastest sealing times occur near the bottom of both major plumes (see a* in Figure 16 and 17). This is where the cold recharge water is in contact with the base of the plume. The temperature range at which precipitation occurs and the fastest sealing times (see equation 8) are given in Table 2. Sealing times along the plume sides in the upper 750 m range between 550-3000 years and 2000-5000 years at 50 and 100 years, respectively (see b* in Figures 16 and 17).

For the central-heated model with layer 2A at 50 years, Figure 18b shows that regions of anhydrite precipitation lie along the sides of the two symmetrical plumes and along the middle plume. The isotherms of temperature distribution of the system are shown in Figure 18a. As in the simulation without layer 2A, the areas with the fastest sealing times for a 100% reduction in porosity occur near the bottom of both major plumes (see a* in Figure 18b). The temperature range at which precipitation occurs and the fastest sealing times are given in Table 2. Sealing times along the plume sides in the upper 750 m (see b* in Figure 18b) range between 80-3000 years.

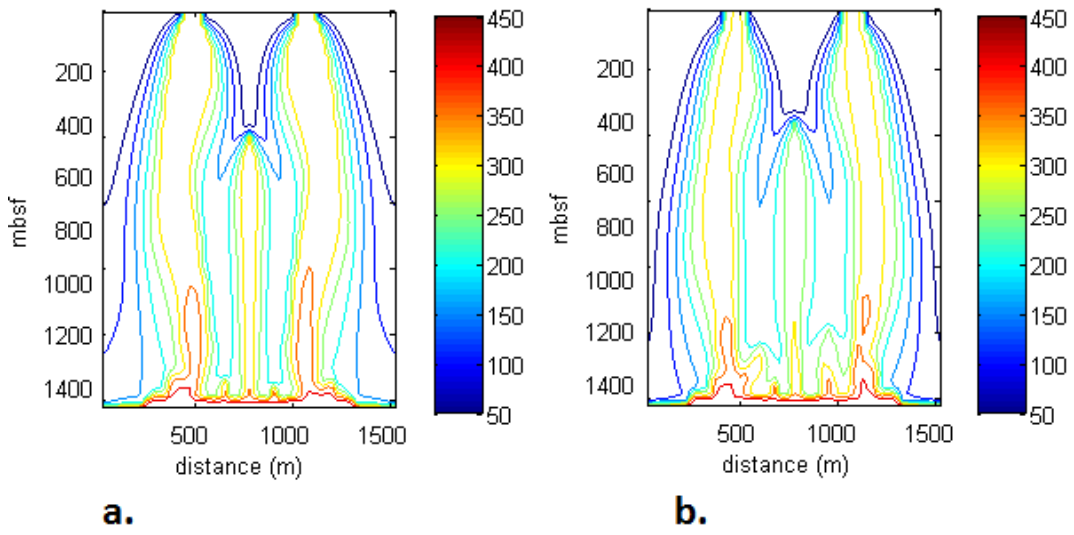

Figure 15. Temperature Distribution isotherms of centrally heated model at a. 50years b. 100years

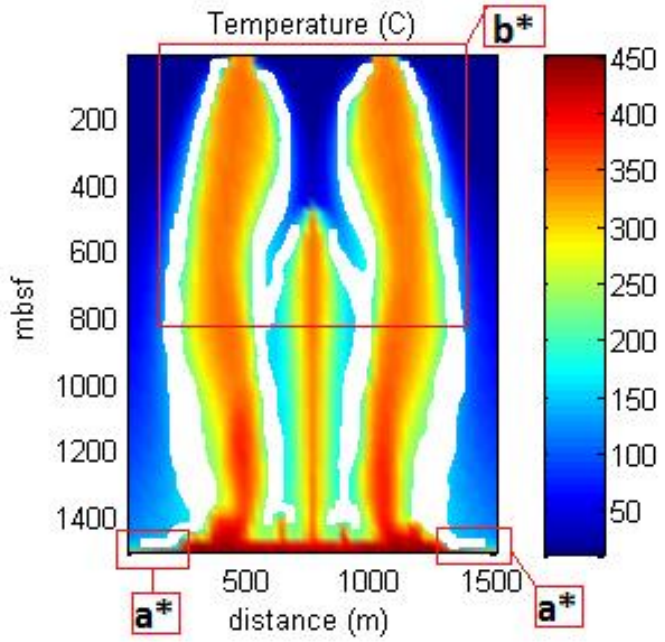

Figure 16. Plot of temperature distribution at 50 years of centrally heated model without layer 2A showing anhydrite precipitation zones in white. a* indicates the zone with fastest sealing times; b* indicates the zone with sealing times ranging from 550-3000 years.

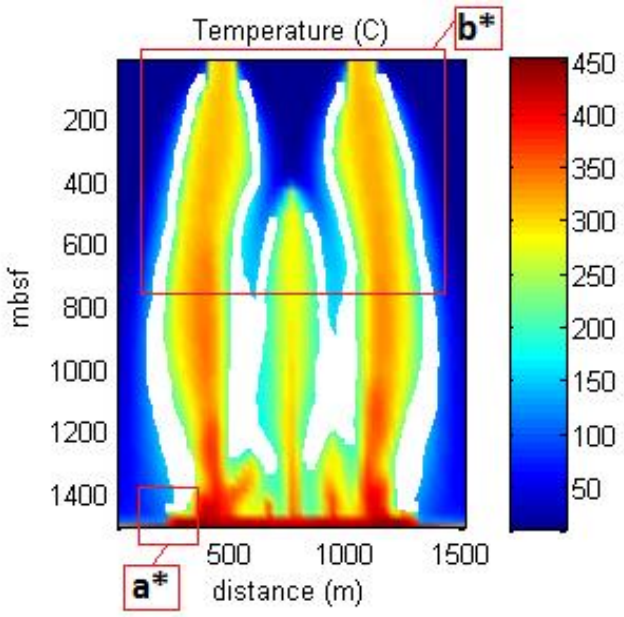

Figure 17. Plot of temperature distribution at 100 years of centrally heated model without layer 2A showing anhydrite precipitation zones in white. a* indicates the zone with fastest sealing times; b* indicates the zone with sealing times ranging from 2000-5000 years.

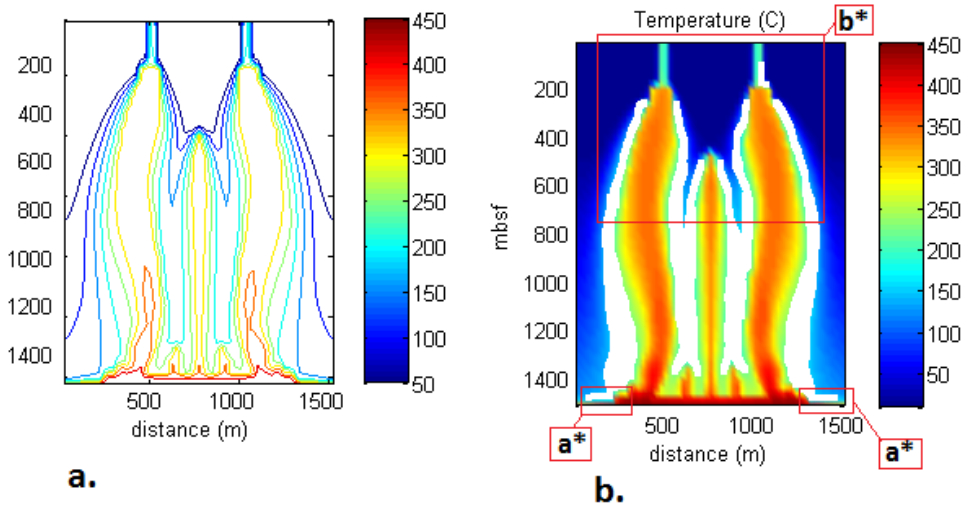

Figure 18. a. Temperature Distribution isotherms at 50years for a centrally heated model with layer 2A; b. Plot of temperature distribution at 50 years of centrally heated model with layer 2A showing anhydrite precipitation zones in white. a* indicates the zone with fastest sealing times; b* indicates the zone with sealing times ranging from 80-3000 years.

Table 2. Fastest sealing times and their temperature ranges for central-heated system (without and with layer 2A) at different snapshots in time

System	Time at Snapshot (years)	Temperature Range	Fastest Sealing Time for 50% Porosity Reduction	Fastest Sealing Time for 100% Porosity Reduction
Central-Heated without Layer 2A	50	~150-170 °C	~35-225years	~70-450years
Central-Heated without Layer 2A	100	~150-190 °C	~190-315years	~380-625years
Central-Heated with Layer 2A	50	~150-170 °C	~20-215years	~55-430years

6. Discussion

6.1. Anhydrite Precipitation and Hydrothermal Recharge at EPR 9°50'N

The results in section 5 show the fastest sealing times occur near the bottom of the deep recharge zones at the sides of the central-heated region. This is where the 150 °C isotherm approximately lies at the base of the recharge zone. This result is similar to the single pass model calculations [e.g., *Lowell et al*., 2012], except that sealing occurs within ~1 year, which is much shorter than given by the numerical results. The main reason appears to be that in the 2-D model the temperature gradients are not nearly as steep as calculated in 1D model [*Lowell et al.*, 2012]. This is partly a result of the 2D character of the flow, but it likely results in part from the resolution of the numerical simulation that is imposed by the assumed cell size of 25 m. To

address the issue of resolution, we ran simulations of the model shown in Figure 10a with the cell sizes of 50 m, 75 m and 100m. The results of these simulations are given in the Appendix A.

To highlight the impact of cell size, Figure 19 shows the fastest sealing times as a function of cell size. The data fits a smooth curve. By extrapolating the curve to smaller cell sizes Figure 19 indicates that sealing would occur after approximately 80 years, if the cell size of the simulations were reduced to 10 m.

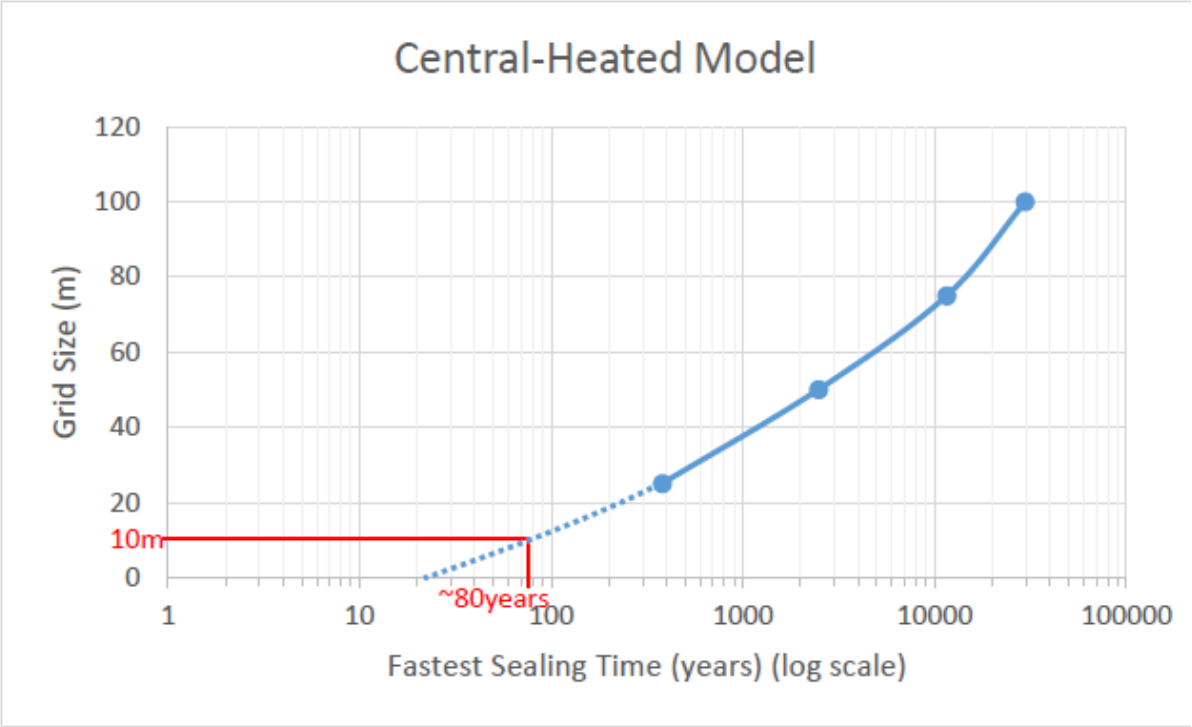

Figure 19. Plot of the fastest sealing time in years (log scale) as a function of grid size in meters. Dotted lines show the extension of the plot to the x-axis. ~80years is the fastest sealing time when extrapolating the sealing time for 10m grid size

Figure 19 shows that even if the cell size were 10 m, the sealing time would be around 80 years, which is still approximately 2 orders of magnitude slower than estimated from the 1D model of *Lowell et al.* [2012]. These results are based on the precipitation of anhydrite from seawater and do not account for the calcium-magnesium exchange from the water-rock reaction,

which would increase the rate of porosity decrease by a factor of three. Moreover, a 50% reduction in porosity would decrease the permeability by approximately one order of magnitude (see equation 9), which would affect circulation pathways. Thus the fluid would tend to flow around areas where porosity and permeability were reduced. This would also result in cooler fluid entering the plume and possibly resulting in lower vent temperature and heat output. These results also assume that the porosity of the crust is 0.1 everywhere. If porosity of the lower crust were smaller, more rapid sealing would occur (see equations 7 and 8).

The numerical results suggest that on a time scale of a decade, anhydrite precipitation in the recharge zone may not significantly affect fluid flow and hydrothermal heat output, thus supporting the hypothesis of *Tolstoy et al.* [2008] that recharge to the EPR 9°50' N hydrothermal system is focused near the 4th order axial discontinuity near 9°49' N. A more detailed analysis of the effect of anhydrite precipitation on hydrothermal recharge requires a numerical simulation in which anhydrite precipitation, and its effects on porosity and permeability, are incorporated more directly. Simulations using a finer grid (e.g., 10 m and 5 m cells), especially near the base of the circulation model, that include water-rock reaction would provide better estimates of the effects of anhydrite precipitation on hydrothermal circulation at EPR 9°50'N.

6.2. Anhydrite Precipitation and Flow Focusing

Anhydrite precipitation along the sides of the plumes tends to maintain the focused high temperature venting and result in higher vent temperatures by reducing the influx of cold seawater into the ascending hot fluids. The reduced mixing would also lead to fluids venting with salinity more reflective of phase separation conditions at depth. The shallow mixing of seawater with the hot fluids in layer 2A could lead to anhydrite precipitation resulting in the formation of an impermeable barrier [*Lowell et al.,* 2007; *Wilcock*, 1998]. This barrier would tend to allow

diffuse hydrothermal discharge to occur relatively near to high temperature vents. The timeframes for sealing estimated from the numerical simulations shown here are quite long, however, suggesting that this process is relatively inefficient when compared to the timescales of years or less as per two branch single-pass hydrothermal circulation model calculations by *Lowell et al.* [2003].

7. Conclusions and Recommendations for Future Work

We have constructed a 2D two-phase hydrothermal circulation model heated from below with parameters that approximate the hydrothermal system at EPR 9°50' N. We used the results of this model to assess the role of anhydrite precipitation in reducing porosity and permeability of the system. We find that anhydrite precipitations likely occurs near the margins of ascending hydrothermal plumes where cooler single phase seawater mixes with the high temperature plume and near the base of the main recharge zone where downwelling fluid is heated to approximately 300 °C. We find that anhydrite precipitation occurs over a considerable amount of area in the system but the estimated sealing times range anywhere from 55-5000years. The fastest sealing times range between 55-625years near the base of the system, whereas longer sealing times occur where seawater mixes with high-temperature rising plumes.

The slow sealing times produced by the 2D numerical model, compared to the 1D analytical simulations support the hypothesis that hydrothermal recharge at EPR 9°50'N may be focused near the 4^{tth} order axial discontinuity near 9°49' N, at least on a decadal time scale, however, the numerical simulations presented here contain a number of simplifications that need to be addressed.

The calculations assume an initial porosity of 0.1 and the porosity at the base of the sheeted dikes may be considerably less than this. The calculations of sealing time are based on the model

structure captured as a snapshot at particular times, which in our cases are 50 and 100 years, when the system has reached a quasi-steady state. This is a preliminary step and a more advance approach would be one where the anhydrite precipitation is incorporated in the code with the porosity and permeability changes along with the precipitation are added as a feedback relative to the previous time step. Another step would be to model the system with a higher temperature at the base (500 °C). This could yield vent temperatures and salinities that are closer to observations at the EPR 9°50'N. Running all the above mentioned simulations and ones with higher basal temperature in smaller cell sizes (12.5 m and 10 m) would refine the calculations leading to more accurate sealing times. That would add more validation points to the plot shown in Figure 19.

Moreover, complete sealing is not required to affect the fluid circulation. Changing the permeability near the base of the cell by an order of magnitude may cause the flow to bypass these regions, thus limiting the impact of anhydrite precipitation on the overall circulation pattern. But this possibility needs further study. By incorporating a high permeability barrier in the fastest sealing zones to one could explore the effect of partial sealing on the evolution of the plume and its temperatures.

One of the main recommendations for future work stemming from this project is to incorporate the anhydrite precipitation in FISHES. This would require integrating temperature and time-dependent anhydrite precipitation into existing set of equations and relating that to permeability and porosity variation with time. This will ultimately provide a clearer picture of how the permeability of the system changes with time.

References

Bai, W., W. Xu, and R. P. Lowell, 2003, The dynamics of submarine geothermal heat pipes, *Geophys. Res. Lett., 30(3), 1108, doi:10.1029/2002GL016176.*

Baross, J.A. and S.E. Hoffman, 1985, Submarine hydrothermal vents and associated gradient environments as sites for the origin and evolution of life. *Origins of Life and Evolution of the Biosphere, 1985, Volume 15, Number 4, Page 327*

Bear, J., 1972, Dynamics of Fluids in Porous Media, *764 pp., Elsevier Sci., New York.*

Bischoff , J. L., and F. W. Dickson, 1975, Seawater-basalt interaction at 200˚C and 500 bars: Implications for origin of seafloor heavy metal deposits and regulation of seawater chemistry, *Earth Planet. Sci. Lett., 25, 385–397.*

Bischoff, J.L., and R. Rosenbauer, 1984, The critical point and two-phase boundary of seawater, 200° - 500 °C, *Earth Planet. Sci. Lett., 68, 172-180.*

Bischoff, J. L., and W. E. Seyfried, 1978, Hydrothermal chemistry of seawater from 25 to 350˚C, *Am. J. Sci., 278, 838–860.*

Blounot, C. W., and F. W. Dickson, 1969, The solubility of anhydrite (CaSO 4) in NaCl-H 2 O from 100 to 450 C and 1 to 1000 bars, *Geochimica et Cosmochimica Acta 33, no. 2 : 227-245.*

Carbotte, S.M., M. Marjanovic, H. Carton, J.C. Mutter, J.P. Canales, M.R. Nedimovic, S. Han, and M.R. Perfit, 2013, Fine-scale segmentation of the crustal magma reservoir beneath the East Pacific Rise, *Nature Geosci. Lett., doi: 10.1038/NGEO1933.*

Coumou, D., T. Driesner, & C.A. Heinrich, 2008, The structure and dynamics of mid-ocean ridge hydrothermal systems, *Science, 321(5897), 1825-1828.*

Degens, E.T. and D.A. Ross (eds.), 1969, Hot brines and recent heavy metal deposits in the Red Sea, *New York: Springer-Verlag, p. 600.*

Detrick, R. S., P. Buhl, E. Vera, J. Mutter, J. Orcutt, J. Madsen, and T. Brocher, 1987, Multi-channel seismic imaging of a crustal magma chamber along the East Pacific Rise, *Nature, 326, 35–41.*

Edmond, J.M., C. Measures, R.E. McDuff, L.H. Chan, R. Collier, B. Grant, L.I. Gordon, and J.B. Corliss, 1979, Ridge crest hydrothermal activity and the balances of the major and minor elements in the ocean: The Galapagos data, *Earth and Planetary Science Letters 46: 1–18.*

Elder, J. W., 1965, Physical processes in geothermal areas, in Terrestrial Heat Flow, *Geophys. Monogr., 8, ed. By W. H. K. Lee, 211–239, AGU, Washington, D. C.*

Elderfield, H. and A. Schultz, 1996, Mid-ocean ridge hydrothermal fluxes and the chemical composition of the ocean, *Annual Reviews of Earth and Planetary Science 24: 191–224.*

Faust, C. R., and J. W. Mercer, 1979, Geothermal reservoir simulation: 1. Mathematical models for liquid- and vapor-dominated hydrothermal systems, *Water Resour. Res., 15, 23-30.*

Fontaine, F., W. Wilcock, and D. Butterfield, 2007, Physical controls on the salinity of mid-ocean ridge hydrothermal vent fluids, *Earth Planet. Sci. Lett., 257, 132-145*

Fornari, D., M. Tivey, H. Schouten, M. Perfit, D. Yoerger, A. Bradley, M. Edwards, R. Haymon, D. Scheirer, K. Von Damm, T. Shank and A. Soule, 2004, Submarine Lava Flow Emplacement at the East Pacific Rise 9°50' N: Implications for Uppermost Ocean Crust Stratigraphy and Hydrothermal Fluid Circulation, *Geophys. Monogr., 148, ed. By C.R. German, J. Lin, and L.M. Parson, 187–218, AGU, Washington, D. C.*

Fornari, D.J., K.L. Von Damm, J.G. Bryce, J.P. Cowen, V. Ferrini, A. Fundis, M.D. Lilley, G.W. Luther III, L.S. Mullineaux, M.R. Perfit, M.F. Meana-Prado, K.H. Rubin, W.E. Seyfried Jr., T.M. Shank, S.A. Soule, M. Tolstoy, and S.M. White, 2012, The East Pacific Rise between 9°N and 10°N: Twenty-five years of integrated, multidisciplinary oceanic spreading center studies, *Oceanography 25(1):18–43, http://dx.doi.org/10.5670/oceanog.2012.02.*

Germanovich, L. N., R. P. Lowell, and P. Ramondenc, 2011, Magmatic origin of hydrothermal response to earthquake swarms: Constraints from heat flow and geochemical data at 9°50′ N, East Pacific Rise, *J. Geophys Res., 116, B05103, doi:10.1029/2009JB006588.*

Goss, A. R., M. R. Perfit, W. I. Ridley, K. H. Rubin, G. D. Kamenov, S. A. Soule, A. Fundis, and D. J. Fornari, 2010, Geochemistry of lavas from the 2005‐2006 eruption at the East Pacific Rise, 9°46′ N‐9°56′ N: Implications for ridge crest plumbing and decadal changes in magma chamber compositions, *Geochem. Geophys. Geosyst., 11, Q05T09, doi:10.1029/2009GC002977.*

Han, L., R. P. Lowell, and K. C. Lewis, 2013, The dynamics of two-phase hydrothermal systems at a seafloor pressure of 25 MPa, *J. Geophys. Res. Solid Earth, 118, 2635–2647, doi:10.1002/jgrb.50158.*

Haymon, R.M., D.J. Fornari, M.H. Edwards, S.M. Carbotte, D. Wright, and K.C. Macdonald, 1991, Hydrothermal vent distribution along the East Pacific Rise crest (9°09'-54'N) and its relationship to magmatic and tectonic processes on fast-spreading mid-ocean ridges, *Earth Planet. Sci. Lett., 104, 513-534.*

Haymon, R. M., D.J. Fornari, K.L. Von Damm, M.D. Lilley, M.R. Perfit, J.M. Edmond, W.C. Shanks III, R.A. Lutz, J.M. Grebmeier, S. Carbotte, D. Wright, E. McLaughlin, M. Smith, N. Beedle, and E. Olson, 1993, Volcanic eruption of the mid-ocean ridge along East Pacific Rise

crest at 9°45’–52’N: Direct submersible observations of seafloor phenomena associated with an eruption event in April 1991, *Earth Planet. Sci. Lett., 119, 85–101.*

Jannasch, H.W., 1983, Microbial processes at deep sea hydrothermal vents. In: Rona PA, Bostrom K, Laubier L, and Smith KL (eds.) Hydrothermal processes at seafloor spreading centers, *NATO Conf. Ser. IV, Mar. Sci.12: pp. 677–710. NY: Springer.*

Jannasch, H.W., 1985, The chemosynthetic support of life and the microbial diversity at deep-sea hydrothermal vents, *Proceedings of the Royal Society London, B 225: 277–297.*

Jannasch, H.W., 1995, Microbial interactions with hydrothermal fluids. In: Humphris SE, Zierenberg RA, Mullineaux LS, and Thomson RE (eds.) Seafloor hydrothermal systems, *Geophysical Monograph Series91: pp. 273–296. Washington, DC: Amer. Geophys. Union.*

Johnson, H. P., M. A. Tivey, T. A. Bjorklund, and M. S. Salmi, 2010, Hydrothermal circulation within the Endeavour Segment, Juan de Fuca Ridge, *Geochem. Geophys. Geosyst., 11, Q05002, doi:10.1029/2009GC002957.*

Kent, G.M., A.J. Harding, and J.A. Orcutt, 1993, Distribution of Magma beneath the East Pacific Rise between the Clipperton Transform and the 9°17'N Deval from Forward Modeling of Common Depth Point Data, *J. Geophys. Res., Vol.98 No.B8, Pg. 13,945-13,969.*

Lewis, K., 2007, Numerical modeling of two-phase flow in the sodium chloride-water system with applications to seafloor hydrothermal systems, *Ph.D. thesis, Ga. Inst. Of Technol., Atlanta.*

Lewis, K. C., and R. P. Lowell, 2009a, Numerical modeling of two-phase flow in the NaCl-H2O system: Introduction of a numerical method and benchmarking, *J. Geophys. Res., 114, B05202, doi:10.1029/2008JB006029.*

Lewis, K.C. and R.P. Lowell, 2009b, Numerical modeling of two-phase flow in the NaCl-H2O system II: Examples, *J. Geophys. Res., 114, B08204, doi:10.1029/2008JB006030.*

Lilley, M. D., D. A. Butterfield, E. J. Olson, J. E. Lupton, S. A. Macko, and R. E. McDuff, 1993, "Anomalous CH4 and NH4+ concentrations at an unsedimented mid-ocean-ridge hydrothermal system, *Nature 364, no. 6432, pg 45-47.*

Lowell, R. P., and D. K. Burnell, 1991, Mathematical modeling of conductive heat transfer from a freezing convecting magma chamber to a single-pass hydrothermal system: Implications for sea floor black smokers, *Earth Planet. Sci. Lett., 104, 59-69.*

Lowell, R.P., P.V. Cappellen, and L.N. Germanovich, 1993, Silica Precipitation in Fractures and the Evolution of Permeability in Hydrothermal Upflow Zones, *American Association for the Advancement of Science, Vol. 260, No. 5105, 192-194.*

Lowell, R. P., and Y. Yao, 2002, Anhydrite precipitation and the extent of hydrothermal recharge zones at ocean ridge crests, *J. Geophys. Res., 107(B9), 2183, doi:10.1029/2001JB001289, 2002.*

Lowell, R. P., Y. Yao, and L. N. Germanovich, 2003, Anhydrite precipitation and the relationship between focused and diffuse flow in seafloor hydrothermal systems, *J. Geophys. Res., 108(B9), 2424, doi:10.1029/2002JB002371.*

Lowell, R.P. and L.N. Germanovich, 2004, Seafloor hydrothermal processes: Results from scale analysis and single-pass models, in Mid-Ocean Ridges: Hydrothermal interactions between the lithosphere and oceans, *Geophys. Monogr., 148, ed. By C.R. German, J. Lin, and L.M. Parson, 219-244, AGU, Washington, D. C.*

Lowell, R. P., S. Gosnell, and Y. Yang, 2007, Numerical simulations of single-pass hydrothermal convection at mid-ocean ridges: Effects of the extrusive layer and temperature-dependent permeability, *Geochem. Geophys. Geosyst., 8, Q10011, doi:10.1029/2007GC001653.*

Lowell, R.P., A. Farough, L.N. Germanovich, L.B. Hebert, and R. Horne, 2012, A vent-field-scale model of the East Pacific Rise 9°50'N magma-hydrothermal system, *Oceanography 25(1):158–167, http://dx.doi.org/10.5670/oceanog.2012.13.*

Lowell, R. P., A. Farough, J. Hoover, and K. Cummings, 2013, Characteristics of magma-driven hydrothermal systems at oceanic spreading centers. *Geochemistry, Geophysics, Geosystems, 14(6), 1756-1770.*

Lowell R.P., K. Kolandaivelu and P.A. Rona, 2014, Hydrothermal Activity, *Reference Module in Earth Systems and Environmental Sciences, Elsevier, 2014. 18-July-14 doi: 10.1016/B978-0-12-409548- 9.09132-6.*

Macdonald, K. S., D.S. Scheirer, & S.M, Carbotte, 1991, Mid-ocean ridges: Discontinuities, segments and giant cracks, *Science, 253(5023), 986.*

Miller, A.R., 1964, Highest salinity in the world ocean?, *Nature 203: 590–591.*

Miller, A.R., 1969, Atlantis II account. In: Degens ET and Ross DA (eds.) *Hot brines and recent heavy metal deposits in the Red Sea, pp. 15–17, New York: Springer-Verlag.*

Miller, A.R., C.D, Densmore, E.T. Degens, R. Pocklington, and A. Jokela, 1966, Hot brines and recent iron deposits in deeps of the Red Sea. *Geochimica et Cosmochimica Acta 30: 341–359.*

Mottl, M. J., 1983, Metabasalts, axial hot springs, and the structure of hydrothermal systems at mid-ocean ridges, *Geol. Soc. Am. Bull., 94, 161–180.*

Nisbet E.G., and N.H. Sleep, 2001, The habitat and nature of early life, *Nature 409: 1083–1091.*

Pascoe, A.R. and J.R. Cann, 1995, Modeling diffuse hydrothermal flow in black smoker vent fields. In: Parson LM, Walker CL, and Dixon DR (eds.), *Hydrothermal vents and processes, pp. 159–173. London: Geological Society, Special Publication No. 87.*

Patankar, S.V. (1980), Numerical Heat Transfer and Fluid Flow, *McGraw-Hill, New York.*

Phillips, O. M., 1991, Flow and Reactions in Permeable Rocks, Pg. 277, *Cambridge Univ. Press, New York.*

Robie, Richard A., Philip M. Bethke, Martha S. Toulmin, and Jerry L. Edwards, 1966, "SECTION 5: X-RAY CRYSTALLOGRAPHIC DATA, DENSITIES, AND MOLAR VOLUMES OF MINERALS." *Geological Society of America Memoirs97, pg: 27-74.*

Ramondenc, P., L.N. Germanovich, K.L. Von Damm, and R.P. Lowell, 2006, The first measurements of hydrothermal heat output at 9°50'N, East Pacific Rise, *Earth Planet. Sci. Lett., 245, 487-497, doi: 10.1016/j.epsl.2006.03.023.*

Sclater, J.G., C. Jaupart, and D. Galson, 1980, The heat flow through oceanic and continental crust and the heat loss of the Earth, *Reviews of Geophysics 18: 269–311.*

Seyfried, W. E., Jr., and J. L. Bischoff, 1981, Experimental seawater-basalt interaction at 300 C, 500 bars, chemical exchange, secondary mineral formation and implication for the transport of heavy metals, *Geochim. Cosmochim. Acta, 45, 135– 147.*

Shanks, W. C., J. K. Böhlke, & R. R. Seal, 1995, Stable Isotopes in Mid-Ocean Ridge Hydrothermal Systems: Interactions Between Fluids, Minerals, and Organisms, in *Seafloor Hydrothermal Systems: Physical, Chemical, Biological, and Geological Interactions (eds S. E. Humphris, R. A. Zierenberg, L. S. Mullineaux and R. E. Thomson), American Geophysical Union, Washington, D. C.. doi: 10.1029/GM091p0194*

Sleep, N. H., 1991, Hydrothermal circulation, anhydrite precipitation and thermal structure at ridge axes, *J. Geophys. Res., 96, 2375–2387.*

Soule, S.A., D.J. Fornari, M.R. Perfit and K.H. Rubin, 2007, New insights into mid-ocean ridge volcanic processes from the 2005-2006 eruption of the East Pacific Rise, 9 degrees 46'N-9 degrees 56'N, *Geology (Boulder)(December 2007), 35(12):1079-1082.*

Tolstoy, M., J. P. Cowen, E. T. Baker, D. J. Fornari, K. H. Rubin, T. M. Shank, & B. Glazer, 2006, A sea-floor spreading event captured by seismometers. *Science, 314(5807), 1920-1922.*

Tolstoy, M., F. Waldhauser, D.R. Bohnenstiehl, R.T. Weekly, and W.-Y. Kim, 2008, Seismic identification of along axis hydrothermal flow on the East Pacific Rise, *Nature, 451, 10, doi: 10.1038/nature06424.*

Waldhauser, F., and M. Tolstoy, 2011, Seismogenic structure and processes associated with magma inflation and hydrothermal circulation beneath the East Pacific Rise at 9°50'N, *Geochem. Geophys. Geosyst., 12, Q08T10, doi:10.1029/2011GC003568.*

Westall F, D. Loizeau, F. Foucher, N. Bost, M. Betrand, J. Vargo, and G. Kminek, 2013, Habitability on mars from a microbial point of view, *Astrobiology 13: 887–897. http://dx.doi.org/ 10.1089/ast.2013.1000.*

White, S. M., R. M. Haymon, and S. Carbotte, 2006, A new view of ridge segmentation and near-axis volcanism at the East Pacific Rise, 8°–12°N, from EM300 multibeam bathymetry, *Geochem. Geophys. Geosyst., 7, Q12O05, doi:10.1029/2006GC001407.*

Wolery, T.J. and N.H. Sleep, 1976, Hydrothermal circulation and geochemical flux at mid-ocean ridges, *Journal of Geology 84: 249–275*

Appendix A: Simulations of Middle Heated Model with Different Cell Sizes

To address the issue of the impact of resolution of the model on sealing times, we ran the model shown in Figure 11a with different cell sizes. The cell sizes are 50 m, 75 m and 100 m along with the 25 m shown in Figure 13.

Figure A.1, A.2 and A.3 shows the temperature distribution of the system at 100 years with 50 m, 75 m and 100 m cell sizes respectively. We can observe the coarseness in the resolution when compared to the temperature distribution at 100 years for a 25 m cell size simulation (see Figure 13d).

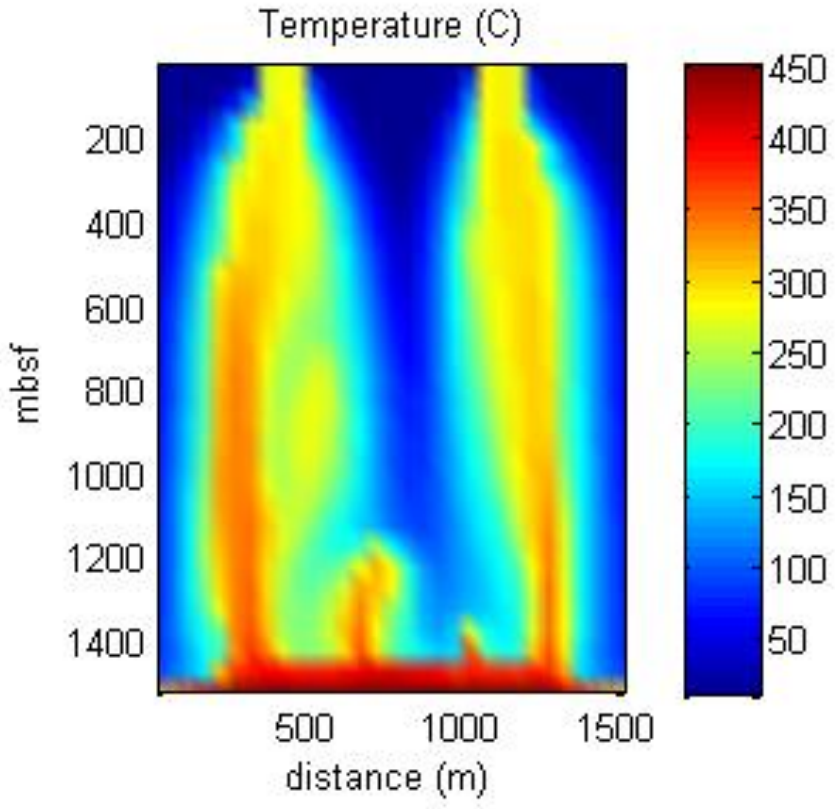

Figure A.1. Temperature distribution at 100 years for a 50 m cell size for a middle heated system

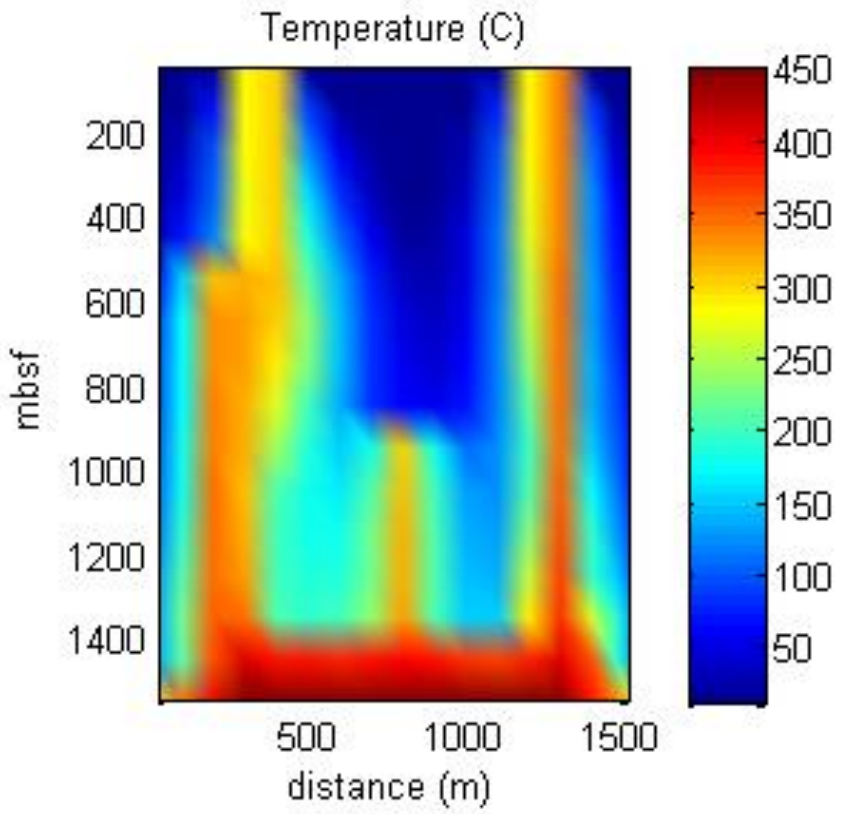

Figure A.2. Temperature distribution at 100 years for a 75 m cell size for a middle heated system

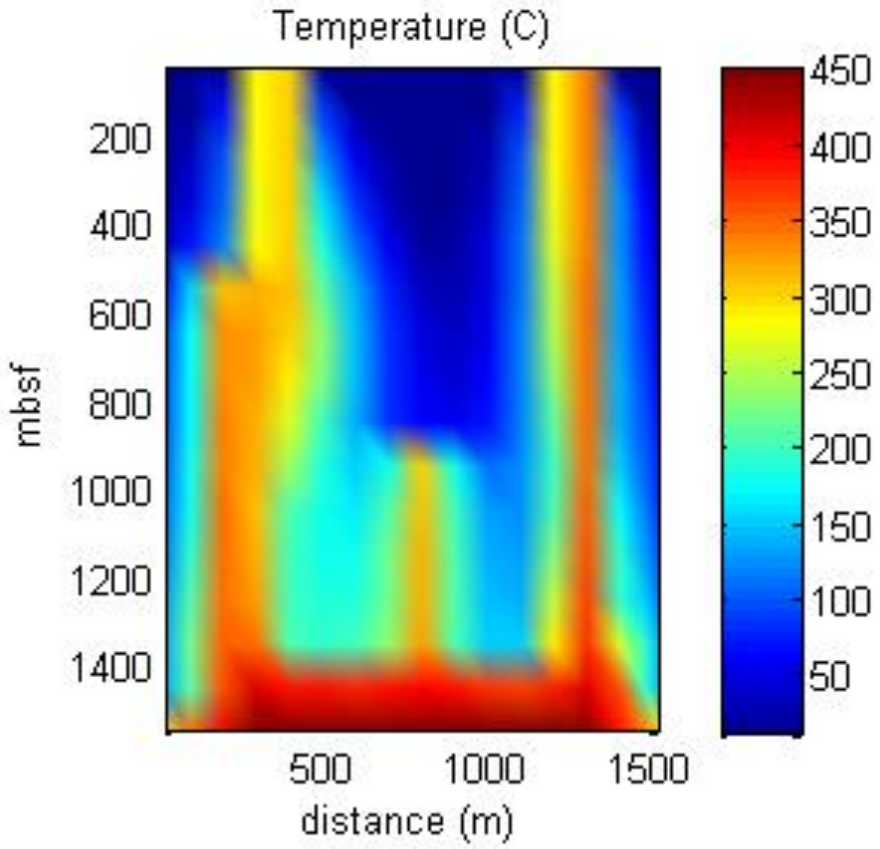

Figure A.3. Temperature distribution at 100 years for a 100 m cell size for a middle heated system